

1
2
3
4
5
6
7
8
9
10
11
12
13
14
15
16
17
18
19
20
21
22
23
24
25
26
27
28
29
30
31
32
33
34
35
36
37
38
39
40
41
42
43
44
45
46
47
48
49
50
51
52
53
54
55
56
57
58
59
60

1 **New insights into North Sea deep crustal structure and extension from** 2 **transdimensional ambient noise tomography**

3
4 1 **E. Crowder^{1,*}, N. Rawlinson², D. G. Cornwell¹, C. Sammarco¹, E. Galetti³, A. Curtis^{3,4}**

5
6
7 2
8 3
9 4 1. School of Geosciences, University of Aberdeen, Aberdeen AB24 3UE, Scotland,
10 5 United Kingdom

11 6
12 7 2. Department of Earth Sciences, University of Cambridge, Cambridge, CB3 0EZ,
13 8 United Kingdom

14 9 3. School of Geosciences, University of Edinburgh, Edinburgh, EH8 9XP, United
15 10 Kingdom

16 11 4. Institute of Geophysics, ETH Zurich, Zurich, Switzerland
17 12
18 13
19 14

20 15 Abbreviated title: Crustal S-wave velocity model of the North Sea from ambient seismic
21 16 noise
22 17

23 18 * Corresponding author. Email address: emily.crowder@abdn.ac.uk (E. Crowder)
24 19
25 20
26 21

22 21 **Summary**

23 22 The deep crustal structure beneath the North Sea is poorly understood since it is
24 23 constrained by only a few seismic reflection and refraction profiles. However, it is widely
25 24 acknowledged that the mid to lower crust plays important roles in rift initiation and evolution,
26 25 particularly when large scale sutures and/or terrane boundaries are present, since these inherited
27 26 features can focus strain or act as inhibitors to extensional deformation. Ancient tectonic
28 27 features are known to exist beneath the iconic failed rift system of the North Sea, making it an
29 28 ideal location to investigate the complex interplay between pre-existing regional heterogeneity
30 29 and rifting. To this end, we produce a 3D shear-wave velocity model from transdimensional
31 30 ambient seismic noise tomography to constrain crustal properties to ~30 km depth beneath the
32 31 North Sea and its surrounding landmasses. Major North Sea sedimentary basins appear as low
33 32 shear-wave velocity zones that are a good match to published sediment thickness maps. We
34 33 constrain relatively thin crust (13-18 km) beneath the Central Graben depocentres that contrasts

1
2
3 34 with crust elsewhere at least 25-30 km thick. Significant variations in crustal structure and rift
4
5 35 symmetry are identified along the failed rift system that appear to be related to the locations of
6
7 36 Laurentia-Avalonia-Baltica paleo-plate boundaries. We constrain first-order differences in
8
9 37 structure between paleo-plates; with strong lateral gradients in crustal velocity related to
10
11 38 Laurentia-Avalonia-Baltica plate juxtaposition and reduced lower crustal velocities in the
12
13 39 vicinity of the Thor suture, possibly representing the remnants of a Caledonian accretionary
14
15 40 complex. Our results provide fresh insight into the pivotal roles that ancient terranes can play
16
17 41 in the formation and failure of continental rifts and may help explain the characteristics of other
18
19 42 similar continental rifts globally.
20

21 43

22 44 **Keywords**

23 45 Seismic tomography

24 46 Seismic noise

25 47 Continental tectonics: extensional

26 48 Crustal structure

27 49 Europe

28 50

29 51 **1. Introduction**

30
31
32 52 Continental regions subject to extensional stresses may eventually rift as the lithosphere
33
34 53 becomes stretched and thinned. If extension continues, a continental rift can ultimately achieve
35
36 54 full breakup and transition to seafloor spreading; yet this stage is often never reached, and a
37
38 55 new mid-ocean rift does not form. The reasons why some rifts fail and others succeed are
39
40 56 unclear; however, the mechanical strength and presence of pre-existing heterogeneity,
41
42 57 including old sutures and faults, may be of primary importance. Understanding failed rift
43
44 58 systems is crucial for understanding how plate tectonics operate on Earth more generally, but
45
46 59 there is also an economic consideration in the form of the vast reserves of oil and gas that they
47
48 60 host (e.g. Bass Strait, Australia; Benue Trough, Nigeria and the North Sea). While the structure
49
50 61 of the uppermost crust and its extensional faulting, basin formation and hydrocarbon reservoirs
51
52 62 tends to be well mapped and understood in these areas, below the economic basement the
53
54 63 deeper crust remains poorly constrained. This is particularly true of the North Sea, where only
55
56 64 a handful of vintage, deep seismic reflection/refraction profiles of varying quality have been
57
58
59
60

1
2
3 65 collected and interpreted (e.g. Pharaoh, 1999). Yet, if we are to understand how rifts form and
4
5 66 why they fail, it is crucial to be able to link upper crustal observations with mid-lower crustal
6
7 67 properties and rift geometry, and their interaction, in order to assess the influence of pre-
8
9 68 existing structures on rift initiation and evolution.

10 69 Prior to the formation of the North Sea, the northwest European Atlantic margin
11
12 70 recorded a long and complex tectonic history. As summarised by Ziegler (1990), numerous
13
14 71 extensional and orogenic events influenced the region since its initial formation during the
15
16 72 triple plate collision of palaeo-continent in the Ordovician-early Devonian Caledonian
17
18 73 Orogeny. This occurred when the Thor Ocean between Avalonia and Baltica closed by
19
20 74 southward subduction under the north Avalonian margin (Torsvik and Rehnström, 2003).
21
22 75 Subsequently, oceanic subduction switched northward beneath the Laurentian margin as
23
24 76 Baltica-Avalonia moved towards Laurentia, closing the Iapetus Ocean in the late Silurian-early
25
26 77 Devonian. Following the triple plate collision, there was widespread sedimentation in the
27
28 78 Devonian as the newly formed Caledonian mountain ranges were eroded. Subsequently,
29
30 79 extension in the Carboniferous resulted in crustal thinning, subsidence and successive sediment
31
32 80 accumulation. From the Triassic to the Jurassic, most of Europe was subject to the main rifting
33
34 81 stage of the North Sea and several kilometres of sediment accumulated in some basins. During
35
36 82 the Cretaceous, rifting ceased, and subsidence slowed, creating the North Sea failed rift system
37
38 83 as the dominant regional stresses shifted westward towards North America and the Proto-
39
40 84 Atlantic opening (e.g. Afari et al. 2018). The location and continuity of ancient collisional
41
42 85 sutures and spatial extent of old/deep extensional zones are uncertain and remain open to debate
43
44 86 (e.g. Smit et al., 2016). Moreover, the failed rifting events in the North Sea overprint and
45
46 87 therefore complicate interpretation of these older, but important crustal features.

47
48 88 To develop a better understanding of North Sea crustal structure and the potential
49
50 89 interplay of ancient sutures and continental rifting, we use ambient noise tomography to create
51
52 90 the first 3D shear-wave velocity model of the crust beneath the North Sea region. Prior to this
53
54 91 work, the North Sea has been included in large-scale regional tomographic studies of Europe
55
56 92 (e.g. Yang et al., 2007), where the horizontal resolution varies from ~100 km in the
57
58 93 southernmost North Sea to >800 km in the central North Sea and is therefore only characterised
59
60 94 by one or two broad scale velocity anomalies. In this study, we present a more detailed model
95
96 95 of the crust to ~30 km depth in which numerous well-constrained features are recovered and
97
98 96 interpret the new model in the context of the crustal structure and tectonic evolution of the
99
100 97 region, with a particular focus on the relationship between ancient tectonic structures and
101
102 98 lithospheric extension.

99 2. Data and methods

100 Prior to this study, surface wave velocities were found to be virtually impossible to
101 extract from North Sea ambient noise data using conventional cross-correlation methods due
102 to the high noise levels and complexities of the recovered signal (Galetti et al., 2016; Nicolson
103 et al., 2014). However, by using recently developed processing techniques, we successfully
104 obtain group velocity dispersion measurements, which are then used in a robust Bayesian,
105 hierarchical, transdimensional tomography scheme to produce a new high-resolution model of
106 the 3D shear-wave velocity structure beneath the North Sea.

107 Data for this study come from 54 permanent seismic stations located in countries
108 surrounding the North Sea (Fig. 1). Both between and within the countries' networks there is
109 high variability in terms of sample rate, type of instrument and corner frequency (which can
110 limit the period range used in dispersion analysis). A major challenge for this dataset is the
111 highly attenuative nature of the crust below the North Sea, which has previously been observed
112 to dramatically reduce the signal-to-noise ratio of short (1-10 s) period surface waves (Ventosa
113 et al., 2017). In the 1-2 s period range, it has been suggested that extremely high attenuation in
114 the North Sea upper crust almost completely suppresses signal in ambient noise cross-
115 correlations (Allmark et al., 2018). In this study, we have a minimum period of 4 s, thereby
116 avoiding the attenuation problem at the shortest periods. Additional challenges arise from the
117 dominant source of noise possibly being within rather than outside the study area (i.e. the
118 Atlantic Ocean was assumed to be the main source, but the North Sea itself may be a significant
119 contributor of microseismic noise – see Nicolson et al., 2014), which can produce spurious
120 arrivals, and hence careful manual cross-checking of waveforms is required. If this is done
121 properly, then this source heterogeneity will otherwise have little effect on narrow band
122 traveltimes measurements in ambient noise tomography (Yao & Van Der Hilst, 2009; Fichtner,
123 2014). In order to obtain high quality surface wave dispersion information, we use
124 approximately five years of continuous data recorded between 2010 and 2015 and apply a new
125 phase-weighted stacking technique (Ventosa et al., 2017), prior to carrying out ambient seismic
126 noise tomography of the North Sea.

127

128 2.1. Preprocessing

129 The ambient noise cross-correlation procedure we employ is similar to that of Bensen
130 et al. (2007), and utilises MSNoise (Lecocq et al., 2014) for data preprocessing. Continuous
131 seismic recordings are split into hour long segments and carefully quality controlled by
132 removing files containing glitches (e.g. data gaps or unexplained spikes) and/or data streams

1
2
3 133 which are less than one-hour duration. To produce the highest quality empirical Green's
4 134 functions, we first remove the mean, the trend and the instrument response from the noise
5 135 recordings of vertical component traces. Subsequently, the mean and trend are removed again,
6 136 and a taper is applied to each trace. The final corrected traces are merged to form files
7 137 containing 24 hours of data (or at least 90% of one full day). All daily traces are down-sampled
8 138 to a uniform 1 sps in order to perform daily cross-correlations.
9
10
11
12
13
14

139

140 **2.2. Stacking**

141 The daily cross-correlations and stacking processes are challenging aspects of this
142 analysis largely due to the fact that the stations surround the North Sea, which itself is likely to
143 be a major source of noise. This creates many artefacts in the cross-correlations that need to be
144 excluded from further analysis. Tests on North Sea data show that phase cross-correlation
145 (Schimmel et al., 2011) is the best approach for de-noising seemingly incoherent signals
146 (Supplementary Fig. 1). To stack all the daily cross-correlations from the entire recording
147 period for each station pair, time-domain phase weighted stacking (ts-PWS, Ventosa et al.,
148 2017) was used (Supplementary Fig. 2). Phase-weighted stacking is a method based on analytic
149 signal theory using the instantaneous phase at each given time on the signal envelope to
150 optimally align traces (this is the phase that should be the same for coherent signals at each
151 given time). When tested against the time-frequency domain PWS (Schimmel et al., 2011),
152 results were very similar, but the ts-PWS was selected as the preferred method based on its
153 significantly higher computational efficiency. A total of 1,275 empirical Green's functions
154 were successfully extracted from the 54-station network (Fig. 2).

155

156 **2.3. Dispersion analysis**

157 We performed group velocity dispersion measurements using a multiple filtering
158 technique (via Computer Programs in Seismology software; Herrmann, 2013) applied to the
159 symmetric component (stack of the causal and acausal signals) of the negative time derivative
160 of the cross-correlation functions, which can be interpreted as Rayleigh wave empirical Green's
161 functions. Group velocities were picked within a period range of 4 – 40 s (Fig. 3), and quality
162 control is implemented via manual inspection of the 1,275 dispersion curves, which were
163 categorised as "good", "fair" and "poor". The "poor" curves were deemed too noisy to pick.
164 The "fair" curves were noisy, but dispersion maxima could be picked with low confidence. The
165 "good" curves had the clearest group velocity dispersion maxima and could be confidently
166 picked. Out of 760 picked dispersion curves, all 614 of the "good" curves are used in the

1
2
3 167 subsequent inversion (Fig. 3). To investigate the feasibility of obtaining phase velocities we
4 168 applied automated frequency-time analysis using the image transformation technique described
5 169 in Young et al. (2011). However, the resultant phase dispersion plots were much noisier and
6 170 less coherent than the equivalent group dispersion plots, which made reliable picking extremely
7 171 challenging (see Supplementary Fig. 3).
8
9
10
11

12 172

13 173 **2.4. Two-stage inversion**

14
15 174 After making the group velocity measurements, a series of tomographic inversions were
16 175 performed for even numbered periods between 4 and 40 s using the transdimensional,
17 176 hierarchical Bayesian inversion technique described by Young et al. (2013). For each period
18 177 of interest, the 2D group velocity model is dynamically parameterised by a tessellation of
19 178 Voronoi cells, which adapt throughout the inversion to the spatially variable data coverage.
20 179 The parameterisation is thus transdimensional in that the number, position, size and velocities
21 180 of the cells are unknowns in the inversion and are implicitly controlled by the data. The
22 181 approach is also considered hierarchical since the level of noise is treated as an unknown in the
23 182 inversion process (Bodin et al., 2012). The aim is to quantify the posterior probability density
24 183 distribution of all model parameters, conditional on the observed data. Out of 500,000 total
25 184 iterations, model unknowns were assumed to have converged after the first 100,000, which
26 185 were discarded as the "burn-in" phase. The remaining models were sifted by taking every 100th
27 186 model, from which the average and standard deviation were calculated across a grid with a
28 187 regular spacing of ~25 km in latitude and longitude (see Supplementary Material for full list of
29 188 prior ranges and parameters). The final results of the inversion are represented by probability
30 189 density functions with the average representing our "preferred" model and the standard
31 190 deviation a measure of uncertainty. While ray trajectories are dependent on phase rather than
32 191 group velocity, it is reasonable to expect that the correlation between phase and group velocity
33 192 is stronger than between group and a constant velocity medium; hence we choose to use ray
34 193 paths dictated by the group velocities rather than great circle paths. This assumption is
35 194 commonly made in group velocity tomography (e.g. Bodin et al., 2012). Ray paths for periods
36 195 10, 20 and 30 s are shown in Fig. 4. With the exception of the region to the west of the Shetland
37 196 Isles, and the other regions outside of our seismometer station network, there is generally
38 197 excellent and even ray path coverage across the vast majority of the North Sea, especially at
39 198 periods > 10 s, and therefore we are confident we sample the main tectonic features in the North
40 199 Sea, albeit within the constraints of the horizontal and vertical resolutions inherent in the
41 200 method.
42
43
44
45
46
47
48
49
50
51
52
53
54
55
56
57
58
59
60

1
2
3 201 With the set of period-dependent group velocity maps from the first stage of the
4
5 202 inversion (Supplementary Fig. 4), we extracted velocity values at a regular grid of points across
6
7 203 the study area in order to generate pseudo 1D group velocity dispersion curves at ~25 km
8
9 204 spacing. These 2,903 curves were then independently inverted for 1D shear-wave velocity
10
11 205 models by using a similar transdimensional, hierarchical Bayesian technique as described
12
13 206 above, and subsequently merged together to create a full 3D model. The 1D shear-wave models
14
15 207 are represented by a set of variable thickness layers, with the number, thickness and velocity
16
17 208 of each layer free to vary during the inversion. The uncertainty estimates for the 2D group
18
19 209 velocity maps were used to weight the input dispersion data in the 1D inversions. This ensures
20
21 210 that noisy measurements (i.e. large standard deviation values) will not unduly influence the
22
23 211 final solution. For each of the 2,903 pseudo-phase velocity dispersion curves, a total of 100,000
24
25 212 model iterations were produced with 50,000 discarded as "burn-in". We found that additional
26
27 213 iterations did not significantly change the average 1D models. Shear-wave velocity was
28
29 214 permitted to vary between 1.5 and 5.0 km/s, and the total number of layers between 2 and 20,
30
31 215 although the natural parsimony of the transdimensional, hierarchical, Bayesian inversion
32
33 216 means that the method tends towards a conservative solution, so an overestimation of velocity
34
35 217 amplitudes is unlikely. The average and standard deviation of each 1D model was used to
36
37 218 construct the final 3D solution model and its associated uncertainty.

38 219

39 220 **2.5. Solution quality and synthetic resolution tests**

40 221 To assess the reliability of group velocity maps produced by the 2D Bayesian inversion
41
42 222 method, we performed a series of resolution tests based on synthetic data. In order to illustrate
43
44 223 the potential recovery of velocity discontinuities and structure at different scales, we applied
45
46 224 the so-called synthetic "checkerboard test". This involved using an identical source-receiver
47
48 225 path configuration to the observational dataset to predict travel-time residuals for a
49
50 226 predetermined checkerboard structure defined by a pattern of alternating high and low velocity
51
52 227 anomalies. Here, we assessed three checkerboard sizes: small ($2.5^\circ \times 1.5^\circ$); medium ($4.0^\circ \times$
53
54 228 2.5°); and large ($5.5^\circ \times 3.5^\circ$), with maximum perturbations of the synthetic velocity anomalies
55
56 229 of ± 0.5 km/s. Gaussian noise with a standard deviation equal to 1 s was added to the synthetic
57
58 230 data to simulate uncertainties associated with the observational dataset (e.g. picking of group
59
60 231 arrival time as a function of period). We used identical source–receiver path combinations to
232 the observational dataset at 10, 20 and 30 s periods; the input structure for each of the three
233 checkerboard sizes are shown in Fig. 4 (left column). The inversion was then carried out using
234 the transdimensional, hierarchical Bayesian scheme.

1
2
3 235 The quality of the recovered checkerboard pattern is generally good (Fig. 5), with
4
5 236 reasonable recovery of the input amplitudes, bearing in mind that there is no regularisation or
6
7 237 preconditioning of the parameterisation (e.g. using the same grid spacing for the synthetic and
8
9 238 recovered models) that is common in conventional linearised methods. By calculating the peak
10
11 239 of each output checkerboard divided by the peak of each input checkerboard, within the North
12
13 240 Sea the smallest size checkerboard test recovers ~55-85%, and the largest checkerboard test
14
15 241 recovers ~65-100%, of the input amplitudes. Smearing of the velocity model is evident in some
16
17 242 places, particularly in regions peripheral to the bounds of the receiver array. For example, the
18
19 243 poor resolution in the north-western corner of the array is due to the station configuration, with
20
21 244 only a single isolated receiver on the Faroe Islands that is somewhat removed from the rest of
22
23 245 the array. However, across the North Sea itself there is some smearing in both NW-SE and NE-
24
25 246 SW directions, but the distortion it causes is not severe. Overall, the checkerboard tests
26
27 247 demonstrated that data from the 54 stations used in this work are capable of resolving features
28
29 248 ~170 km in size with even better recovery in regions of the model with concentrated path
30
31 249 coverage where we might expect smaller features to be better resolved (Fig. 5).

32
33 250 In order to investigate the reliability of the second stage of the transdimensional,
34
35 251 hierarchical, Bayesian inversion, in which pseudo-group-velocity dispersion curves are
36
37 252 inverted for 1D shear velocity models, we performed another synthetic test. A four-layer crustal
38
39 253 shear wave velocity model which includes a low velocity layer was used as the synthetic input
40
41 254 to test the ability of the inversion to recover structure, with Gaussian noise of 0.2 km/s standard
42
43 255 deviation added to the group dispersion data to simulate measurement uncertainty. The quality
44
45 256 of the recovered 1D shear velocity model is generally good; the probability density plot and its
46
47 257 mean are in approximate agreement with the input model (Fig. 6), although the largest
48
49 258 inconsistencies between the synthetic and recovered model occur in the neighbourhood of the
50
51 259 velocity discontinuities. Given that surface waves cannot discriminate between velocity
52
53 260 discontinuities and strong velocity gradients, the fact that the mean solution model produces a
54
55 261 smoothed version of the layered input model is to be expected.

56
57 262

58 59 263 **3. Results**

60
61 264 We present the 3D crustal structure beneath the North Sea region in a series of
62
63 265 horizontal and vertical slices taken from the final tomographic solution. Significant velocity
64
65 266 anomalies that will be interpreted later are numbered on the horizontal slices in Fig. 7. We use
66
67 267 the standard deviation of the model ensemble, computed at each individual grid point in
68
69 268 latitude, longitude and depth, as an estimate of uncertainty (Fig. 8). Regions of high standard

1
2
3
4
5
6
7
8
9
10
11
12
13
14
15
16
17
18
19
20
21
22
23
24
25
26
27
28
29
30
31
32
33
34
35
36
37
38
39
40
41
42
43
44
45
46
47
48
49
50
51
52
53
54
55
56
57
58
59
60

269 deviation can generally be correlated with a lack of path coverage or lack of crossing paths.
270 Because there are no seismic stations beneath the oceans, uncertainty is in general higher
271 offshore compared to onshore. In the following we quote Moho depths based upon the 4.2 km/s
272 contour in our model; the accuracy of our Moho depth estimates will vary according to model
273 uncertainty (Fig. 8) and the sharpness of the S-wave velocity gradient at the base of the crust.
274 A proxy for depth uncertainty that we consider is the average difference between the 4.2 km/s
275 contour and the 4.1 km/s and 4.3 km/s contours. Under this assumption, in offshore regions
276 with a sharp Moho discontinuity a depth uncertainty of ± 2 km is appropriate, whereas
277 onshore with gentler Moho velocity gradients (where we sample the base of the crust) it is
278 likely to be at least ± 4 km.

279 Fig. 7(a) shows a horizontal slice at 4 km depth, which is dominated by low shear-wave
280 velocities across the North Sea. These velocities, which vary between 2.2 and 2.9 km/s, are
281 widespread across northern Germany, the Netherlands, Denmark and through the Central North
282 Sea towards and beyond Shetland and Norway (labelled '1'). A notable area of higher velocity
283 between the lows in the North Sea is a region with velocities of ~ 3.5 km/s to the east of northern
284 England (labelled '2'). At 8 and 11 km depths (Fig. b-c), velocities of 2.8-3.1 km/s span much
285 of the North Sea between the UK and Denmark. This relatively low velocity feature appears to
286 terminate at the UK coastline, but may extend onshore in the east across northernmost Germany
287 (labelled '3'). The horizontal slice at 15 km depth (Fig. 7d) also shows this low velocity
288 anomaly, but here it is confined to the western part of the North Sea, adjacent to the UK. This
289 implies that the anomaly could thicken and/or dip westward. At the eastern end of the depth
290 slices at 11 and 15 km depth (Figs. 7c-d) is an area of elevated velocity in the vicinity of
291 Denmark and southern Sweden (labelled '4'). It is characterised by velocities of ~ 4.1 km/s
292 compared to its surroundings of ~ 3.8 km/s. Fig. 7(d-f) shows horizontal slices at 15, 20 and 25
293 km depth, on which we observe a pronounced zone of velocities > 4.1 km/s that extend and
294 widen northwards from the centre of the North Sea (labelled '5'). This zone is generally
295 surrounded by lower velocities of ~ 3.5 - 3.8 km/s. At 25 km depth (Fig. 7f), this high velocity
296 region appears to widen south of the centre of the North Sea; for example, at $\sim 56^\circ$ N it widens
297 from ~ 170 km at 20 km depth, to ~ 360 km at 25 km depth. This widening is greater in the west
298 of the velocity anomaly than the east. It also broadens with depth further north, where at 59° N
299 the elevated velocities extend from ~ 215 km wide at 20 km depth, to ~ 295 km wide at 25 km
300 depth. At depths of 20 and 25 km (Fig. 7e-f) a second region of very high velocities (> 4.1 km/s)
301 is present below northern Germany (labelled '6'). There appears to be a connection between

1
2
3 302 the high velocities in the northern and central North Sea and those below northern Germany in
4
5 303 a narrow (~100 km) ~N-S trending zone which features velocities of ~4.2 km/s.

6
7 304 Fig. 9(a) shows a vertical slice through our 3D shear velocity model taken at 60° N,
8
9 305 which extends from the west of Shetland to eastern Norway. Assuming crustal velocities are
10
11 306 generally <4.2 km/s (Kennett et al., 1995), we observe thin (~14 km) crust below the Viking
12
13 307 Graben. Overlying the thinnest sections of crust, low velocities (<2.7 km/s) span the North Sea
14
15 308 upper crust from Shetland to Norway (anomaly '1'). We also observe that the crustal velocity
16
17 309 character is significantly different on either side of the thin region. Below Norway, crustal
18
19 310 thickness is likely to be >30 km whereas below the Shetland Plateau it is ~27 km. Furthermore,
20
21 311 on the Norwegian side the velocity properties are apparently more uniform with higher
22
23 312 velocities (mostly >3.4 km/s) throughout, whereas on the Shetland side lower velocities are
24
25 313 more extensive (~3.0 km/s in the upper crust). A vertical slice through our shear velocity model
26
27 314 further south at 56° N (Fig. 9c) highlights other significant features in our results. Again,
28
29 315 assuming a base of crust velocity of 4.2 km/s, we observe that the crustal thickness below
30
31 316 central Scotland is ~30 km, which is in contrast to Denmark and Sweden where mantle
32
33 317 velocities are not reached, implying a crustal thickness of >30 km. Low velocity anomaly '3'
34
35 318 is visible below the North Sea on this vertical slice. These velocities are lower than anywhere
36
37 319 else in our model at these depths. This low velocity anomaly has an apparent westward dip or
38
39 320 alternatively thickens to the west but does not continue below Scotland. The final key feature
40
41 321 to note in this cross-section is the asymmetry of the highly elevated mantle velocities (>4.3
42
43 322 km/s, labelled '5'), which underlie the thin crust below the North Sea (Figs. 9a & 9c). We
44
45 323 observe that these high velocities have a much more abrupt transition to normal crustal
46
47 324 velocities in the east compared with the more gradual transition on the Scottish side.

48 325

49 326 **4. Discussion**

50
51 327 In this section we focus on key features and regions in the new 3D shear-wave velocity
52
53 328 model that are relevant in addressing the link between lithospheric extension and pre-existing
54
55 329 structures, which is the main goal of this study. We have taken care when interpreting features
56
57 330 in our velocity model, particularly in regions where resolution is reduced and uncertainty is
58
59 331 higher (e.g. Figs. 5 & 8), and focus the majority of our discussion on the deep crust where the
60
332 velocity model is best resolved.

333

334

335 4.1. Sedimentary basins and the Mid North Sea High

336

337 In the uppermost crust, shear-wave velocities of 2.2-2.9 km/s are widespread across
338 northern Germany, the Netherlands, Denmark and throughout the North Sea (labelled '1' on
339 Fig. 7a). These low velocities are characteristic of sedimentary basins, typically created by
340 lithospheric extension, and we find their distribution matches well with sediment thickness
341 maps, such as EuCRUST-07 (Tesauro et al., 2008), which is derived from seismic reflection,
342 refraction and receiver function data. However, EuCRUST07 differs markedly from our model
343 in the vicinity of the Mid North Sea High (MNSH), which lies in the Central North Sea between
344 the Northern and Southern Permian Basins and has acted as a relative high since at least
345 Devonian times (e.g. Arsenikos et al., 2019). Here, a distinct area of higher velocity (~3.5 km/s)
346 is observed on the 4 km depth slice of our new model (anomaly '2'; Fig. 7a & 9c), which
347 extends from the northeast coast of England and across the MNSH (Fig. 1), and appears to be
348 confined to the uppermost ~5 km of the crust (Fig. 9c). Gravity studies have been used to map
349 the presence of granites across the area (Wernicke, 1985) and Well 37/25-1 (drilled in 2009 by
350 Esso) penetrated the Dogger High, and found that the crustal blocks likely contain granite
351 cores, which typically exhibit higher shear-wave velocities than the surrounding sedimentary
352 basins. This is especially true if shallow-level crustal intrusions are emplaced and grow through
353 the incremental stacking of sill-like sheets, rather than isolated plutons (e.g. Wilson et al.,
354 2016). The presence of granite throughout the MNSH uppermost crust is therefore a plausible
355 explanation for the elevated velocities in this region. The size of each individual granite pluton
356 is likely to be below the resolving power of our dataset, which may help explain why we
357 observe a diffuse zone of elevated wavespeed (Fig. 5). Another consideration is that several
358 boreholes on the MNSH sampled sedimentary rocks that experienced greenschist and possibly
359 amphibolite facies metamorphism during late Ordovician times (Pharaoh et al., 1995). The
360 laboratory estimated shear-wave velocity of greenschist is 3.57 km/s (Christensen, 1996),
361 which is very close to the ~3.5 km/s shear-wave velocity we find in our model. We therefore
362 suggest that a combination of granite-cored fault blocks and greenschist facies metamorphism
363 explains the widespread elevated S-wave velocities we observe in the upper crust around the
364 MNSH.

365

366

1
2
3 3674
5 368 **4.2. Low velocities in the mid-crust**

6
7 369 A significant volume of unexpectedly low velocities (2.8-3.1 km/s) spans much of the
8
9 370 North Sea between Denmark and the UK, adjacent to the Viking and Central Grabens, and best
10
11 371 identified on the 11 km depth slice (anomaly '3'; Fig. 7c). This relatively low velocity zone
12
13 372 appears to terminate at the eastern UK coastline and is also present on the horizontal model
14
15 373 slice at 15 km depth (Fig. 7d), where it is confined to the western parts of the North Sea. On
16
17 374 cross-section slice B-B' (Fig. 9c), anomaly '3' apparently extends to ~16 km depth, below
18
19 375 which highly elevated velocities of >4.1 km/s exist, most likely indicating moderately thinned
20
21 376 crust below it. We observe relatively higher standard deviation values (therefore greater
22
23 377 uncertainty) in the offshore area, where anomaly '3' is located, than for the onshore area (Fig.
24
25 378 9c-d), and checkerboard resolution tests show that anomalies the size of '3' can be subject to a
26
27 379 degree of smearing (Fig. 4e-h). However, this low velocity region is consistently present in our
30
31 380 Rayleigh wave group period maps and subsequent S-wave velocity model.

28 381 A widespread low P-wave velocity mid-lower crust in the region of anomaly '3' has not
29
30 382 been conclusively shown on previous seismic refraction/wide angle reflection profiles, largely
31
32 383 because only a few sampled the fringes of this anomaly. 3D compilations of velocity models
33
34 384 (e.g. Kelly et al., 2007) show a slightly elevated average crustal velocity in this region, but this
35
36 385 is likely due to the absence of low velocity sedimentary rocks beneath the Mid North Sea High.
37
38 386 However, a low (6.3-6.4 km/s) P-wave velocity zone in the mid- to lower crust either west of
39
40 387 the Central Graben (Nielsen et al., 2000) or following the Caledonian Thor suture zone (Smit
41
42 388 et al., 2016) was constrained on a number of deep seismic reflection and refraction profiles (i.e.
43
44 389 MONALISA profiles 1–3 across the Central Graben; the combined European GeoTraverse
45
46 390 sub-profiles EUGEMI and EUGENO-S 1 and LT-7, PQ-2; and BASIN-9601 profiles across
47
48 391 the Baltica margin), but their locations do not constrain its westward extent. We find that our
49
50 392 model exhibits low S-wave velocities in a similar location as the low P-wave anomalies
51
52 393 described by Smit et al. (2016); however, the match is not perfect, and the low V_S region
53
54 394 extends much further west. Based on the distribution of low V_S in our model, we propose that
55
56 395 this low velocity zone continues much further westwards and could reach the British coastline.
57
58 396 The low P-wave velocities were interpreted by Smit et al. (2016) as a separate crustal unit
59
60 397 consisting of a collapsed Caledonian accretionary complex located between Baltica and
398 Avalonia, who also compared it to the present-day Kuril and Cascadia subduction zones. In
399 these modern cases, broad zones of low (6.4-6.6 km/s) P-wave velocities have been found in

1
2
3
4
5
6
7
8
9
10
11
12
13
14
15
16
17
18
19
20
21
22
23
24
25
26
27
28
29
30
31
32
33
34
35
36
37
38
39
40
41
42
43
44
45
46
47
48
49
50
51
52
53
54
55
56
57
58
59
60

400 the subduction channels and interpreted to be due to either trapped fluids, highly sheared lower
401 crustal rocks, and/or underthrust accretionary rock (e.g. Ramachandran et al. 2006). Further
402 work that examines azimuthal anisotropy from Rayleigh waves, and radial anisotropy using a
403 combination of Rayleigh and Love wave analysis may shed light on the internal properties of
404 this anomaly.

405 Buried Devonian age or older sedimentary rocks may offer an alternative explanation
406 for low velocities in the mid-lower crust (e.g. Arsenikos et al., 2019; Milton-Worsell et al.,
407 2010); however, at depths of up to 16 km, sedimentary material is unlikely to remain un-
408 metamorphosed by high pressures and temperatures. For example, assuming an average
409 geotherm of 23°C/km (Madsen, 1974), the temperature at 15 km depth would be ~345 °C
410 putting the rocks into the greenschist metamorphic facies zone (Yardley, 1989). The laboratory
411 estimated shear-wave velocity of greenschist is 3.57 km/s (Christensen, 1996), making it an
412 unlikely sole candidate for our low shear-wave velocity zone (2.8-3.1 km/s).

413 A number of deep seismic reflection profiles acquired across the North Sea (e.g. BIRPS
414 and SNST83-7; Klemperer et al., 1991) show an unreflective upper- to mid-crust in the same
415 region as our anomaly '3', and (in most cases) it occurs directly above highly reflective lower
416 crust. The high reflectivity itself has been attributed to igneous intrusion but may also represent
417 cross-cutting low-angle structures or other compositional heterogeneity (e.g. Klemperer et al.,
418 1991). If magmatic intrusion followed by expulsion of water from local metamorphism has
419 occurred (*cf.* the Rhine Graben, Wenzel and Sandmeier, 1992), it is possible that migrated
420 fluids trapped in the mid- to upper crust contribute to the unusually low shear wavespeeds
421 below the North Sea. Taking the low shear-wave velocity zone in our model of 2.8-3.1 km/s,
422 and corresponding P-wave velocities of 6.3-6.4 km/s (Smit et al., 2016), this gives an elevated
423 V_p/V_s ratio of approximately 2.2. Low aspect ratio microcracks saturated with incompressible
424 fluid and high pore fluid pressure in laboratory experiments have been shown to have high
425 V_p/V_s close to 2.2 (Wang et al., 2012) and the presence of brines in microcracks and fractures
426 have been proven to exist to depths of at least 12 km at 190 °C and 9 km at 265 °C in the Kola
427 (Russia) and KTB (Germany) boreholes respectively, where the presence of fluids correlated
428 with and helped explain the lowered seismic velocities (Smithson et al., 2000). The implication
429 for our study is that the presence of fluid and microcracks could be a contributing factor to the
430 low shear-wave velocity zone. Further studies to characterise the anisotropy in this region may
431 help to confirm this interpretation, with microcracks expected to open according to the
432 predominantly NW-SE maximum compressive ambient stress field (Heidbach et al., 2010).

433

1
2
3 434 The Caledonian Orogeny involved the subduction of part of the Tornquist Sea basin
4
5 435 beneath Avalonia (Pharaoh et al., 1995), and geophysical evidence indicates that at least two
6
7 436 subduction zones were involved in this process, remnants of which are presently known as the
8
9 437 Thor Suture and the Dowsing-South Hewett Fault Zone. The latter fault zone is a long-lived
10
11 438 NW-SE trending crustal lineament (Fig. 1) and was reactivated throughout late Palaeozoic and
12
13 439 Mesozoic times (Pharaoh, 1999). On deep seismic reflection data it separates crust of distinctly
14
15 440 different seismic reflectivity character, and a south-westerly dipping reflector at the Moho and
16
17 441 upper mantle has been mapped parallel to, and just coastward of the fault zone which may mark
18
19 442 the location of an Ordovician subduction zone and/or crustal suture (Klemperer et al., 1991).
20
21 443 The low velocity zone in our shear-wave velocity model appears to terminate at the Dowsing-
22
23 444 South Hewett Fault Zone (within our resolution limits) and therefore it is plausible that the low
24
25 445 velocity region (anomaly '3') is either constrained or caused by these two ancient subduction
26
27 446 zones.

28 447

29 448 **4.3. Variations in North Sea crustal thinning**

30 449

31
32 450 One of the most striking features of the 3D shear-wave velocity model is a high velocity
33
34 451 zone (>4.3 km/s) that is widest and constrained at ≤ 15 km depth beneath the northern North
35
36 452 Sea (Fig. 7d), narrows southward before widening (with an eastward offset) into the central
37
38 453 North Sea where it occurs at 15-20 km depth (Fig. 7e). These high velocities are likely to be
39
40 454 the result of surface waves sampling the uppermost mantle, which can be defined seismically
41
42 455 as shear-wave speeds >4.3 km/s (e.g. PREM; Dziewonski and Anderson, 1981; AK135;
43
44 456 Kennett et al., 1995) and therefore the shape and characteristics of the region of velocity
45
46 457 anomaly '5' (Figs. 7 and 9) can provide information about the thinned crust due to North Sea
47
48 458 extension and its possible relationship(s) with pre-existing structures.

49 459

50
51 460 The main region of high velocities in the northern North Sea occurs directly beneath
52
53 461 low velocities associated with sedimentary rocks within the Viking graben, as shown on cross-
54
55 462 section A-A' (Fig. 9a). The crust is constrained to be ~ 14 km thick, in contrast to the >30 km
56
57 463 and ~ 27 km to the east and west, respectively, and the width of the region of upper mantle S-
58
59 464 wave velocities is likely to be in the region of 2-300 km. Higher model uncertainty beneath the
60
465 Shetland Islands region precludes detailed interpretation, but we do not appear to reach >4.2
466 km/s and therefore interpret that the Moho defines a symmetrically thinned crust beneath the

1
2
3 467 Viking graben axis, albeit with differing crustal thicknesses representing Laurentia and Baltica
4 468 margins (Fig. 10a). Further south, the central and southern North Sea rifts are characterised by
5 469 a more laterally abrupt transition to lower velocities to the east, compared to a more gradual,
6 470 dipping geometry to the west. This asymmetry in crustal structure is markedly different from
7 471 that further north and can be clearly observed on cross-section B-B' (Fig. 9c). Striking
8 472 observations of crustal thinning in these parts of the North Sea are the large lateral offset
9 473 between near-surface low velocities delineating prominent sedimentary basins (e.g. Fig. 7b)
10 474 and crustal complexity at the Avalonia-Baltica boundary. We therefore show, for the first time
11 475 at this scale, significant changes in geometry along strike of the thinned crust of the North Sea
12 476 rift system that appear related to the pre-existing juxtaposition of ancient paleo-plates. The
13 477 symmetric thinning in the northern North Sea is in contrast to the asymmetric thinning in the
14 478 central and southern North Sea, with the different styles most likely controlled by ancient
15 479 paleo-continent in each location; i.e. extension in lithosphere of Baltica and Laurentia origin
16 480 in the north led to symmetric thinning, while extension in lithosphere of Avalonia and Laurentia
17 481 origin in the south resulted in asymmetric thinning and eventual termination of the North Sea
18 482 failed rift system (Fig. 10).

19 483

20 484 At depths >20 km, a second region of very high velocities (>4.3 km/s) is present below
21 485 northern Germany (anomaly '6'; Fig. 7f). At shallower depths, this is the approximate location
22 486 of the late Jurassic to early Cretaceous age Lower Saxony Basin (Fig. 1). The elevated
23 487 velocities that characterise anomaly '6' are very similar to those of anomaly '5', perhaps
24 488 indicating that this is another area of thinned crust where mantle velocities are being sampled.
25 489 Interestingly, there appears to be some connection between the fast velocities below the Central
26 490 Graben and those below the Lower Saxony Basin in a narrow (~100 km wide) zone of ~N-S
27 491 trending velocities of ~4.2 km/s (Fig. 7e-f). This zone is situated beneath the South-Central
28 492 North Sea Graben and the eastern Netherlands, both areas of substantial Carboniferous-Jurassic
29 493 igneous activity which was coincident with the initial development of the Proto-South Central
30 494 North Sea Graben (Sissingh, 2004). Taking into consideration the resolution of our model (Fig.
31 495 5), we tentatively suggest that the spatial relationship between the igneous activity and elevated
32 496 shear-wave velocity zone could indicate that we are observing the extension of the
33 497 southernmost part of the North Sea failed rift system into northern Germany.

34 498

35 499 **4.4. Deep crustal structure, thinning and structural inheritance**

1
2
3
4 500

5 501 Structural inheritance is a property of continental lithosphere that focusses deformation along
6 502 pre-existing structures, e.g. faults, shear or suture zones (e.g. Schiffer et al., 2019). The
7 503 associated reactivation is primarily controlled by the compositional and mechanical properties
8 504 of the pre-existing structures (e.g. Holdsworth et al., 2001). We use our new S-wave velocity
9 505 model to examine the relationships between the major pre-extensional structures that are
10 506 present in the North Sea, in particular the different paleo-plates and their boundaries, some of
11 507 which are marked by major suture zones, and evidence for crustal thinning (Fig. 11).

12 508 Beneath the northern North Sea, crustal thinning is most pronounced adjacent to the
13 509 presumably resistant Norwegian Baltic Shield and a region of thinned crust underlies the
14 510 Viking Graben and Horda Platform to the east. Further west, thinned crust exists east of the
15 511 Shetland Islands and notably north of the Shetland Platform, which may support the conclusion
16 512 of Fazlikhani et al., (2017) that Devonian tectonic extension occurred over a wide region of the
17 513 northern North Sea.

18 514 The southern extent of the thinnest crust in the northern North Sea changes geometry
19 515 in the vicinity of where the Southern Uplands Fault (SUF), Hardangerfjord Shear Zone (HSZ)
20 516 and possible westward extension of the Sorgenfrei-Tornquist Zone (STZ) congregate, with the
21 517 locus of thinning apparently offset to the east in regions south of the STZ. The thinnest crust
22 518 here varies in lateral extent but is consistent with, for example, the thinnest crust in the
23 519 refraction/gravity/magnetic model (Transect 1) of Williamson et al., 2002, and it primarily
24 520 occurs in a region defined by the STZ to the north, crust that may represent a remnant
25 521 accretionary wedge related to the Thor suture (Smit et al., 2018) to the west and south and the
26 522 Caledonian Deformation Front (CDF) to the east (Fig. 11). The enigmatic crust interpreted by
27 523 Smit et al., (2018) as a remnant Thor suture accretionary wedge (RTAW) could alternatively
28 524 represent a deformed and metamorphosed flake of Avalonia Microplate (Pharaoh et al., 1995),
29 525 or an entirely exotic crustal terrane caught up along the Avalonia/Baltica suture (Coney et al.,
30 526 1980). Interestingly, the Central Graben appears to occur in this crust, where it is underlain by
31 527 moderately thinned crust but is notably to the west of where our model shows elevated deep
32 528 velocities interpreted as the upper mantle at shallowest depths (~15-20 km). This relationship
33 529 may indicate that the crustal ribbon containing the remnant Thor accretionary wedge may
34 530 possess properties that facilitate brittle faulting whilst inhibiting ductile extension.

35 531 The southern extent of the Central Graben that marks the major crustal thinning of the
36 532 Southern North Sea major crustal thinning, as defined by our interpreted mantle S-wave
37 533 velocities, is coincident with where the RTAW (Smit et al., 2016), following the Elbe Line,

1
2
3 534 changes to a more northwest-southeast orientation and hence becomes oblique to the more
4
5 535 north-south axis of the southern North Sea rift (Fig. 11). Overall extension in the North Atlantic
6
7 536 region during Mesozoic times was in an E-W to NW-SE direction (e.g. Ziegler, 1990), which
8
9 537 could indicate that the RTAW's orientation was sub-optimal for rifting to propagate further
10
11 538 southwards. Our S-wave velocity models show an absence of the wide region of high velocity
12
13 539 anomalies at 20 km depth as the rift attempts to cross the RTAW, most likely indicating less
14
15 540 crustal thinning (possibly confined to a ~100 km wide zone) and they reappear beneath the
16
17 541 Lower Saxony Basin in northern Germany.

17 542

18
19 543 In relation to the distribution of paleo-plates in the North Sea, rifting appears to initially follow
20
21 544 the path of least resistance, the weakness that was the suture zone between Laurentia and
22
23 545 Baltica, evidenced by our new 3D velocity model. When it reached the triple plate collision
24
25 546 junction, it changes rifting style, becoming more complex and displaying an offset between
26
27 547 upper crust and whole crust extension (Fig. 10). Our new model shows that rifting was unable
28
29 548 to continue to propagate very far into Avalonian lithosphere, likely because it possesses
30
31 549 different mechanical properties that require greater tectonic forces to extend. Structural
32
33 550 inheritance, and in particular the influence of paleo-plates, plays a key role in rifting and rift
34
35 551 failure. For example, a rift can initially exploit the weakest part of the lithosphere at a paleo-
36
37 552 suture zone. However, if a juxtaposed paleo-plate is mechanically stronger and hence is able
38
39 553 to resist strain localisation, then the rift may cease to propagate and ultimately fail. Our results
40
41 554 provide new evidence of how inherited lithosphere properties, such as suture zones and
42
43 555 variations in mechanical strength, are a fundamental control on rift formation, style,
44
45 556 propagation and termination.

43 557

44 558 **5. Conclusions**

46 559 We present the first 3D shear-wave velocity model of the North Sea region from
47
48 560 ambient seismic noise tomography. Due to noise sources within the North Sea, previous studies
49
50 561 have found it difficult to extract reliable inter-station group velocity dispersion data. However,
51
52 562 by utilising time–frequency domain phase-weighted stacking to improve the signal-to-noise,
53
54 563 we were able to successfully extract robust surface wave dispersion information. A
55
56 564 transdimensional, hierarchical, Bayesian inversion method, which is highly data driven and
57
58 565 requires minimal tuning of initial parameters, was then applied to invert for shear wave
59
60 566 velocity. This approach accounts for heterogeneous data coverage, produces an ensemble of
567 solution models and can constrain data uncertainty parameters. Our main findings include:

1
2
3 568
4

- 5 569
6
7 570
8
9 571
10
11 572
12
13 573
14 574
15
16 575
17
18 576
19
20 577
21 578
22
23 579
24
25 580
26
27 581
28
29 582
30 583
31
32 584
33 585
34
35 586
36
37 587
38
39 588
40
41 589
42 590
43
44 591
45
46 592
47
48 593
49 594
50
51 595
52
53 596
54
55 597
56 598 **Acknowledgments**
57
58 599
59
60 600
- Low velocities (<2.9 km/s) across much of the North Sea, Denmark, the Netherlands and northern Germany which are interpreted as signatures of the major North Sea sedimentary basins and match well with published sediment thickness maps;
 - Relatively higher velocities (~3.5 km/s) in the upper crust of the Mid North Sea High region, typical of granites and greenschist and corresponding to locations of granites inferred from gravity anomalies;
 - Anomalously low velocities (2.8-3.1 km/s) in the upper- to mid-crust in the vicinity of the Thor suture and across the southern North Sea, which could be interpreted as representing the remnants of a Caledonian accretionary complex. Alternatively, they may be caused by the presence of water (and/or microcracks) related to possible magmatic underplating in the area associated with Jurassic rifting in the North Sea;
 - Relatively higher velocities in the vicinity of the Trans European Suture Zone (~4.1 km/s compared to its surroundings of ~3.8 km/s);
 - Significantly elevated velocities (>4.2 km/s) representing thinned (13-18 km) crust beneath the Viking and Central Grabens. Rift style appears to be symmetric in the northern North Sea Viking Graben and strongly asymmetric in the Central Graben. This may be related to the location of the Laurentia-Avalonia-Baltica paleo-plates.
 - Shallow high velocities (>4.2 km/s at 20 km depth, implying thinner crust) below Germany, with a tentative connection to the main North Sea rift system via a narrow N-S trending corridor of high velocities.

Finally, we find that both rifting style (symmetric vs. strongly asymmetric) and propagation ability varies across crust of different paleo-plate origins. We suggest that our new 3D shear-wave velocity model provides evidence of how inherited paleo-plate boundaries and suture zones play a fundamental role in the genesis, evolution and termination of failed continental rifts.

Acknowledgments

The work contained in this paper was conducted during a PhD study undertaken as part of the Natural Environment Research Council (NERC) Centre for Doctoral Training (CDT) in

1
2
3 601 Oil & Gas [grant number NEM00578X/1]. This work was performed using the Maxwell High
4 602 Performance Computing Cluster of the University of Aberdeen IT Service
5 603 (www.abdn.ac.uk/staffnet/research/hpc.php), provided by Dell Inc. and supported by Alces
6 604 Software. Plots were generated with the Generic Mapping Tools or GMT (Wessel et al., 2013).
7
8 605 We thank Nick Schofield and Tim Pharaoh for constructive conversations, which aided the
9 606 interpretation of our results, and Amy Gilligan for her insightful advice during preparation of
10 607 this manuscript. We also thank Richard England and an anonymous reviewer for their
11 608 comments on the original version of the manuscript.
12
13
14
15
16
17
18

19 610 **References**

- 20 Allmark, C., Curtis, A., Galetti, E., de Ridder, S., 2018. Seismic attenuation from ambient noise
21 across the North Sea Ekofisk permanent array. *Journal of Geophysical Research: Solid*
22 *Earth* 123, 8691–8710.
23
24
25
26 Arsenikos, S., Quinn, M., Kimbell, G., Williamson, P., Pharaoh, T., Leslie, G., Monaghan, A.,
27 2019. Structural development of the Devonian-Carboniferous plays of the UK North Sea.
28 *Geological Society, London, Special Publications* 471, 65–90.
29 <https://doi.org/10.1144/SP471.3>
30
31
32
33 Audet, P., Bostock, M.G., Christensen, N.I., Peacock, S.M., 2009. Seismic evidence for
34 overpressured subducted oceanic crust and megathrust fault sealing. *Nature* 457, 76.
35
36 Bensen, G.D., Ritzwoller, M.H., Barmin, M.P., Levshin, A.L., Lin, F., Moschetti, M.P.,
37 Shapiro, N.M., Yang, Y., 2007. Processing seismic ambient noise data to obtain reliable
38 broad-band surface wave dispersion measurements. *Geophysical Journal International*
39 169, 1239–1260.
40
41
42
43 Bezacier, L., Reynard, B., Bass, J.D., Sanchez-Valle, C., Van de Moortèle, B., 2010. Elasticity
44 of antigorite, seismic detection of serpentinites, and anisotropy in subduction zones. *Earth*
45 *and Planetary Science Letters* 289, 198–208.
46
47
48 Bodin, T., Sambridge, M., Rawlinson, N., Arroucau, P., 2012. Transdimensional tomography
49 with unknown data noise. *Geophys J Int* 189, 1536–1556. [https://doi.org/10.1111/j.1365-](https://doi.org/10.1111/j.1365-246X.2012.05414.x)
50 [246X.2012.05414.x](https://doi.org/10.1111/j.1365-246X.2012.05414.x)
51
52
53 Christensen, N., 1996. Poisson's ratio and crustal seismology. *Journal of Geophysical*
54 *Research: Solid Earth* 101, 3139–3156.
55
56 Coney, P.J., Jones, D.L., Monger, J.W., 1980. Cordilleran suspect terranes. *Nature* 288, 329.
57
58 Dziewonski, A.M., Anderson, D.L., 1981. Preliminary reference Earth model. *Physics of the*
59 *earth and planetary interiors* 25, 297–356.
60

- 1
2
3 Fazlikhani, H., Fossen, H., Gawthorpe, R. L., Faleide, J. I., and Bell, R. E. (2017), Basement
4 structure and its influence on the structural configuration of the northern North Sea rift,
5 *Tectonics*, 36, 1151– 1177, doi:10.1002/2017TC004514.
6
7
8 Fichtner, A., 2014. Source and processing effects on noise correlations. *Geophysical Journal*
9 *International*, 197(3), pp.1527-1531.
10
11 Galetti, E., Curtis, A., Baptie, B., Jenkins, D., Nicolson, H., 2016. Transdimensional Love-
12 wave tomography of the British Isles and shear-velocity structure of the East Irish Sea
13 Basin from ambient-noise interferometry. *Geophysical Journal International* 208, 36–58.
14
15 Gibson, G.M., Totterdell, J., Morse, M.P., Goncharov, A., Mitchell, C.H., Stacey, A.R., 2012.
16 Basement Structure and Its Influence on the Pattern and Geometry of Continental Rifting
17 and Breakup Along Australia’s Southern Rift Margin. *Geoscience Australia*.
18
19 Heidbach, O., Tingay, M., Barth, A., Reinecker, J., Kurfeß, D., & Müller, B. (2010). Global
20 crustal stress pattern based on the World Stress Map database release 2008.
21 *Tectonophysics*, 482(1-4), 3–15. doi:10.1016/j.tecto.2009.07.023
22
23 Herrmann, R.B., 2013. Computer programs in seismology: An evolving tool for instruction and
24 research. *Seismological Research Letters* 84, 1081–1088.
25
26 Holdsworth, R.E., Stewart, M., Imber, J., Strachan, R.A., 2001. The structure and rheological
27 evolution of reactivated continental fault zones: a review and case study. *Geological*
28 *Society, London, Special Publications* 184, 115–137.
29
30 Ji, S., Li, A., Wang, Q., Long, C., Wang, H., Marcotte, D., Salisbury, M., 2013. Seismic
31 velocities, anisotropy, and shear-wave splitting of antigorite serpentinites and tectonic
32 implications for subduction zones. *Journal of Geophysical Research: Solid Earth* 118,
33 1015–1037.
34
35 Kelly, A., England, R.W. and Maguire, P.K.H. (2007), A crustal seismic velocity model for
36 the UK, Ireland and surrounding seas. *Geophysical Journal International*, 171: 1172-1184.
37 doi:10.1111/j.1365-246X.2007.03569.x
38
39 Kennett, B.L., Engdahl, E.R., Buland, R., 1995. Constraints on seismic velocities in the Earth
40 from traveltimes. *Geophysical Journal International* 122, 108–124.
41
42 Klemperer, S.L., 1988. Crustal thinning and nature of extension in the northern North Sea from
43 deep seismic reflection profiling. *Tectonics* 7, 803–821.
44
45 Klemperer, S.L., Hobbs, R., Hobbs, R.W., 1991. *The BIRPS Atlas: Deep Seismic Reflections*
46 *Profiles Around the British Isles*. Cambridge University Press.
47
48 Kodaira, S., 2004. High Pore Fluid Pressure May Cause Silent Slip in the Nankai Trough.
49 *Science* 304, 1295–1298. <https://doi.org/10.1126/science.1096535>
50
51
52
53
54
55
56
57
58
59
60

- 1
2
3 Lecocq, T., Caudron, C., Brenguier, F., 2014. MSNoise, a python package for monitoring
4 seismic velocity changes using ambient seismic noise. *Seismological Research Letters* 85,
5 715–726.
6
7
8 Lister, G.S., Etheridge, M.A., Symonds, P.A., 1991. Detachment models for the formation of
9 passive continental margins. *Tectonics* 10, 1038–1064.
10
11 Madsen, L., 1974. Approximate geothermal gradients in Denmark and the Danish North Sea
12 sector. *Danm. Geol. Unders. \Aarbog for* 5–16.
13
14 McKenzie, D., 1978. Some remarks on the development of sedimentary basins. *Earth and*
15 *Planetary science letters* 40, 25–32.
16
17 Milton-Worssell, R., Smith, K., McGrandle, A., Watson, J., Cameron, D., 2010. The search for
18 a Carboniferous petroleum system beneath the Central North Sea. *Petroleum Geology*
19 *Conference series* 7, 57–75. <https://doi.org/10.1144/0070057>
20
21
22
23
24 Nicolson, H., Curtis, A., Baptie, B., 2014. Rayleigh wave tomography of the British Isles from
25 ambient seismic noise. *Geophysical Journal International* 198, 637–655.
26
27 Nielsen, L., Balling, N., Jacobsen, B. H., and MONA LISA Working Group (2000). Seismic
28 and gravity modelling of the crustal structure in the Central Graben, North Sea:
29 Observations along MONA LISA profile 3. *Tectonophysics*, 328, 229–244.
30
31 Peacock, S.M., Christensen, N.I., Bostock, M.G., Audet, P., 2011. High pore pressures and
32 porosity at 35 km depth in the Cascadia subduction zone. *Geology* 39, 471–474.
33
34
35 Pharaoh, T., England, R., Lee, M., 1995. The concealed Caledonide basement of Eastern
36 England and the southern North Sea — A review. *Stud Geophys Geod* 39, 330–346.
37
38 <https://doi.org/10.1007/BF02295826>
39
40 Pharaoh, T.C., 1999. Palaeozoic terranes and their lithospheric boundaries within the Trans-
41 European Suture Zone (TESZ): a review. *Tectonophysics* 314, 17–41.
42
43 [https://doi.org/10.1016/S0040-1951\(99\)00235-8](https://doi.org/10.1016/S0040-1951(99)00235-8)
44
45
46 Ramachandran, K., Hyndman, R.D., Brocher, T.M., 2006. Regional P-wave velocity structure
47 of the Northern Cascadia Subduction Zone. *J. Geophys. Res.* 111, n/a-n/a.
48
49 <https://doi.org/10.1029/2005JB004108>
50
51 Schiffer, C., Doré, A.G., Foulger, G.R., Franke, D., Gernigon, L., Holdsworth, B., Kusznir, N.,
52 Lundin, E., Peace, A., Petersen, K.D., Phillips, T., Stephenson, R., Stoker, M.S., Welford,
53 K., 2019. Structural inheritance in the North Atlantic 81.
54
55
56 Schimmel, M., Stutzmann, E., Gallart, J., 2011. Using instantaneous phase coherence for signal
57 extraction from ambient noise data at a local to a global scale. *Geophysical Journal*
58 *International* 184, 494–506.
59
60

- 1
2
3 Sissingh, W., 2004. Palaeozoic and Mesozoic igneous activity in the Netherlands: a
4 tectonomagmatic review. *Netherlands Journal of Geosciences* 83, 113–134.
5
6 Smit, J., van Wees, J.D., Cloetingh, S., 2016. The Thor suture zone: From subduction to
7 intraplate basin setting. *Geology* 44, 707–710. <https://doi.org/10.1130/G37958.1>
8
9
10 Smithson, S.B., Wenzel, F., Ganchin, Y.V., Morozov, I.B., 2000. Seismic results at Kola and
11 KTB deep scientific boreholes: velocities, reflections, fluids, and crustal composition.
12 *Tectonophysics* 329, 301–317.
13
14
15 Stratford, W., Thybo, H., Faleide, J.I., Olesen, O. and Tryggvason, A., 2009. New Moho map
16 for onshore southern Norway. *Geophysical Journal International*, 178(3), pp.1755-1765.
17
18 Tesauro, M., Kaban, M.K., Cloetingh, S.A., 2008. EuCRUST-07: A new reference model for
19 the European crust. *Geophysical Research Letters* 35.
20
21
22 Thybo, H., Maguire, P.K.H., Birt, C., Perchuc, E., 2000. Seismic reflectivity and magmatic
23 underplating beneath the Kenya Rift. *Geophysical Research Letters* 27, 2745–2748.
24
25
26 Torsvik, T.H., Rehnström, E.F., 2003. The Tornquist Sea and Baltica–Avalonia docking.
27 *Tectonophysics* 362, 67–82.
28
29
30 Ventosa, S., Schimmel, M., Stutzmann, E., 2017. Extracting surface waves, hum and normal
31 modes: time-scale phase-weighted stack and beyond. *Geophysical Journal International*
32 211, 30–44.
33
34
35 Wang, X.-Q., Schubnel, A., Fortin, J., David, E.C., Guéguen, Y., Ge, H.-K., 2012. High Vp/Vs
36 ratio: Saturated cracks or anisotropy effects? *Geophysical Research Letters* 39.
37 <https://doi.org/10.1029/2012GL051742>
38
39
40 Wenzel, F., Sandmeier, K.-J., 1992. Geophysical evidence for fluids in the crust beneath the
41 Black Forest, SW Germany. *Earth-Science Reviews* 32, 61–75.
42
43
44 Wernicke, B., 1985. Uniform-sense normal simple shear of the continental lithosphere.
45 *Canadian Journal of Earth Sciences* 22, 108–125.
46
47
48 Wessel, P., Smith, W.H., Scharroo, R., Luis, J., Wobbe, F., 2013. Generic mapping tools:
49 improved version released. *Eos, Transactions American Geophysical Union* 94, 409–410.
50
51
52 Williamson, J.P., Pharaoh, T.C., Banka, D., Thybo, H., Laigle, M., Lee, M.K. Potential field
53 modelling of the Baltica–Avalonia (Thor-Tomquist) suture beneath the southern North
54 Sea, *Tectonophysics*, 360 (1–4) (2002), pp. 47-60
55
56
57 Wilson, P.I.R., McCaffrey, K.J.W., Wilson, R.W., Jarvis, I., Holdsworth, R.E., 2016.
58 Deformation structures associated with the Trachyte Mesa intrusion, Henry Mountains,
59 Utah: Implications for sill and laccolith emplacement mechanisms. *Journal of Structural*
60 *Geology* 87, 30–46. <https://doi.org/10.1016/j.jsg.2016.04.001>

- 1
2
3 Yamasaki, T., Gernigon, L., 2009. Styles of lithospheric extension controlled by underplated
4 mafic bodies. *Tectonophysics* 468, 169–184.
5
6 Yang, Y., Ritzwoller, M.H., Levshin, A.L., Shapiro, N.M., 2007. Ambient noise Rayleigh wave
7 tomography across Europe. *Geophysical Journal International* 168, 259–274.
8
9 Yardley, B.W., 1989. An introduction to metamorphic petrology.
10
11 Yao, H. and Van Der Hilst, R.D., 2009. Analysis of ambient noise energy distribution and
12 phase velocity bias in ambient noise tomography, with application to SE Tibet.
13 *Geophysical Journal International*, 179(2), pp.1113-1132.
14
15 Young, M.K., Rawlinson, N., Arroucau, P., Reading, A.M., Tkalčić, H., 2011. High-frequency
16 ambient noise tomography of southeast Australia: New constraints on Tasmania’s tectonic
17 past. *Geophysical Research Letters* 38. <https://doi.org/10.1029/2011GL047971>
18
19 Young, M.K., Rawlinson, N., Bodin, T., 2013. Transdimensional inversion of ambient seismic
20 noise for 3D shear velocity structure of the Tasmanian crust. *Geophysics* 78, WB49–
21 WB62.
22
23 Ziegler, P.A., 1990. Geological atlas of western and central Europe. Geological Society of
24 London.
25
26
27
28
29
30
31
32
33
34
35
36
37
38
39
40
41
42
43
44
45
46
47
48
49
50
51
52
53
54
55
56
57
58
59
60

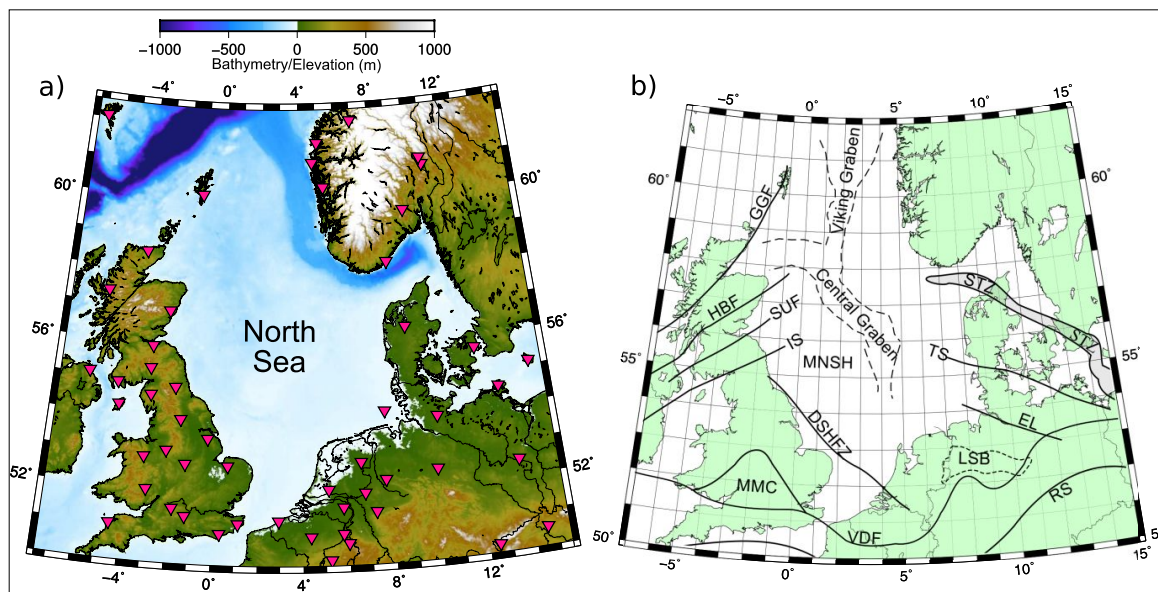


Fig. 1: Map of the North Sea and surrounding regions showing (a) seismometers used in this study (red triangles); and (b) major crustal features in the study area. GGF: Great Glen Fault; HBF: Highland Boundary Fault; SUF: Southern Uplands Fault; IS: Iapetus Suture; MNSH: Mid-North Sea High; DSHFZ: Dowsing South Hewett Fault Zone; MMC: Midlands Micro-craton; VDF: Variscan Deformation Front; LSB: Lower Saxony Basin; RS: Rheic Suture; EL: Elbe Lineament; TS: Thor Suture; STZ: Sorgenfrei-Tornquist Zone.

1
2
3
4
5
6
7
8
9
10
11
12
13
14
15
16
17
18
19
20
21
22
23
24
25
26
27
28
29
30
31
32
33
34
35
36
37
38
39
40
41
42
43
44
45
46
47
48
49
50
51
52
53
54
55
56
57
58
59
60

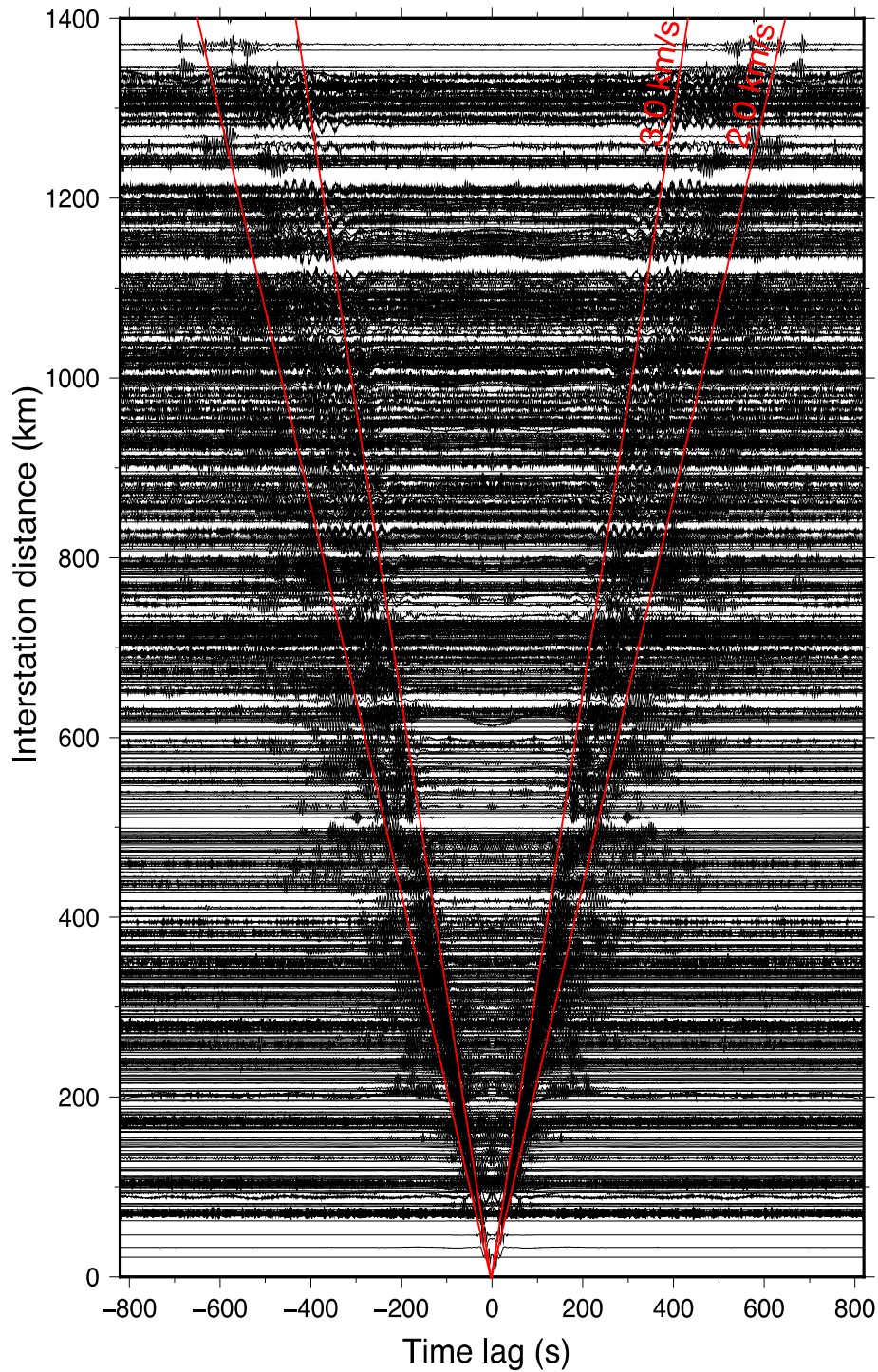


Fig. 2: Final cross-correlations (symmetric component) for all simultaneously recording station pairs used for group velocity dispersion analysis, obtained from phase weighted stacking, plotted as a function of interstation distance. The red lines are plotted to highlight moveout velocities of 2 km/s and 3 km/s.

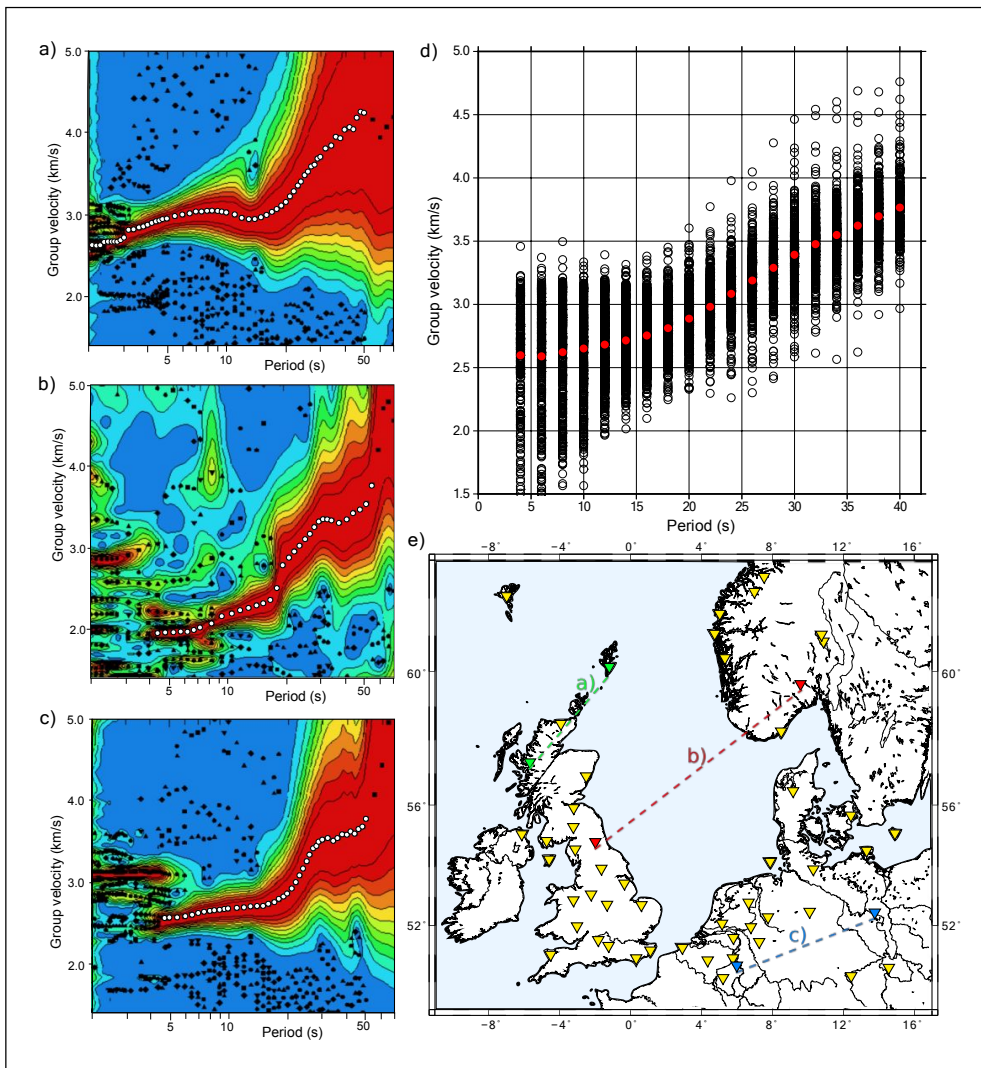


Fig. 3: (a-c) Plots showing group velocity dispersion curves computed from cross-correlations between the three station pairs shown in (e), with white dots denoting the group dispersion picks; (d) dispersion data from all 614 “good” curves, with the average for each period shown in red.

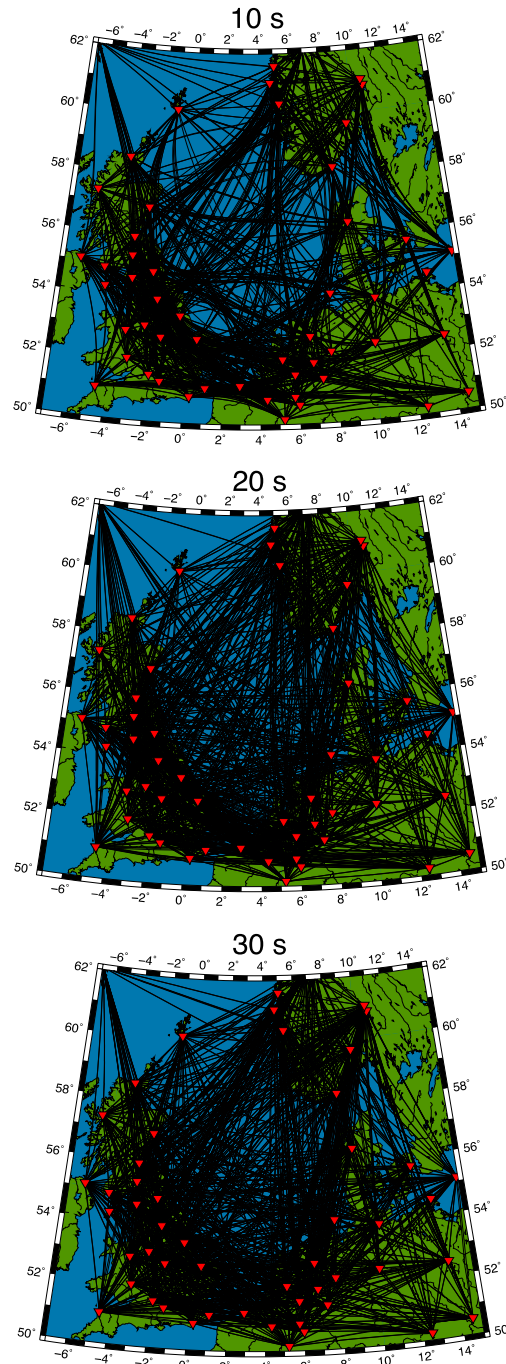


Fig. 4: Ray paths for 10, 20 and 30 s periods, with red triangles showing the location of seismometer stations used in this project.

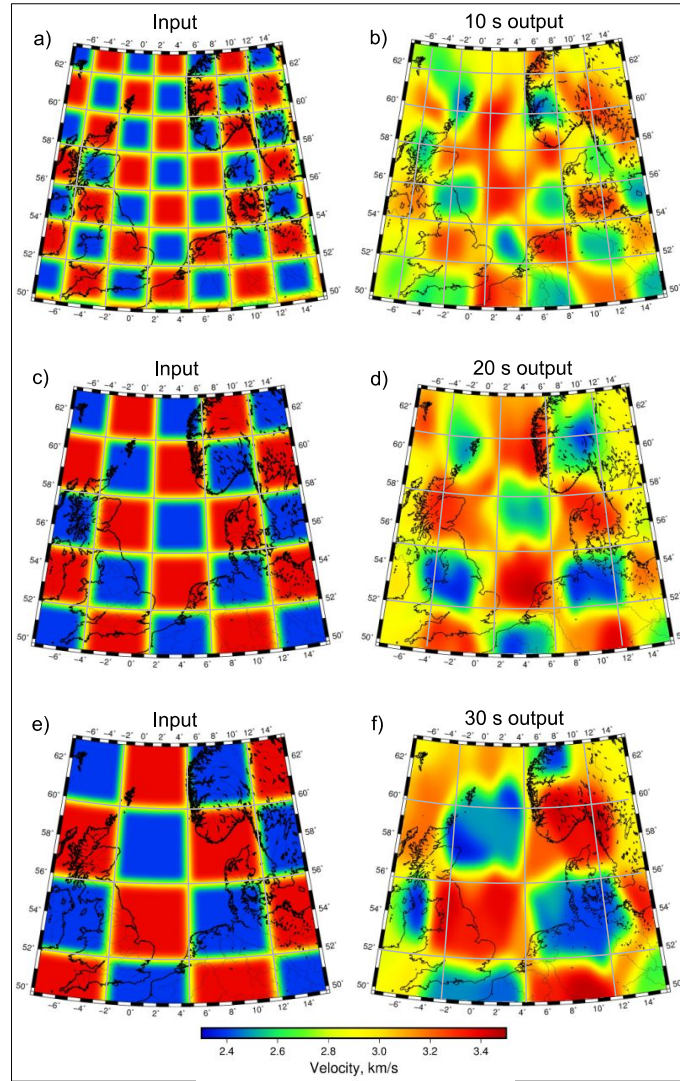


Fig. 5: Checkerboard resolution tests for velocity structure recovery using transdimensional, hierarchical, Bayesian inversion. Synthetic input velocities are input as small, medium and large size checkerboard patterns. Output velocity models (right) for optimum recovery periods. See supplementary Fig. 2 for outputs from all periods. Grey lines overlaid for visual comparison.

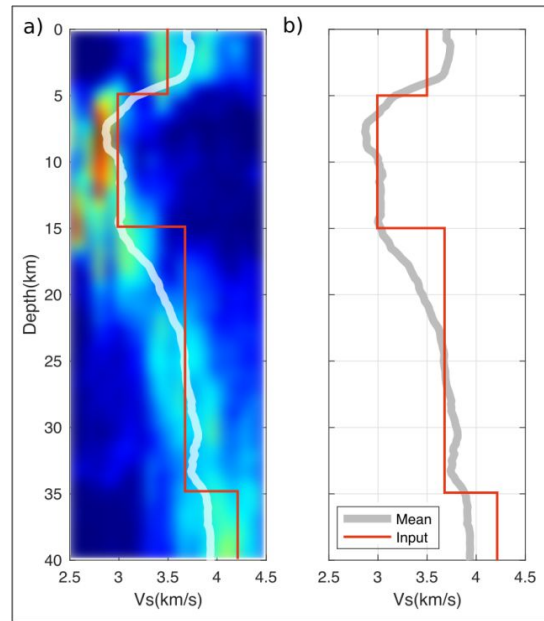


Fig. 6: Results of a synthetic recovery test for 1D crustal shear velocity structure. Red solid line denotes the input model that we attempt to recover. (a) Probability density plot; red is high probability and blue is low probability; (b) mean of the recovered velocity distribution.

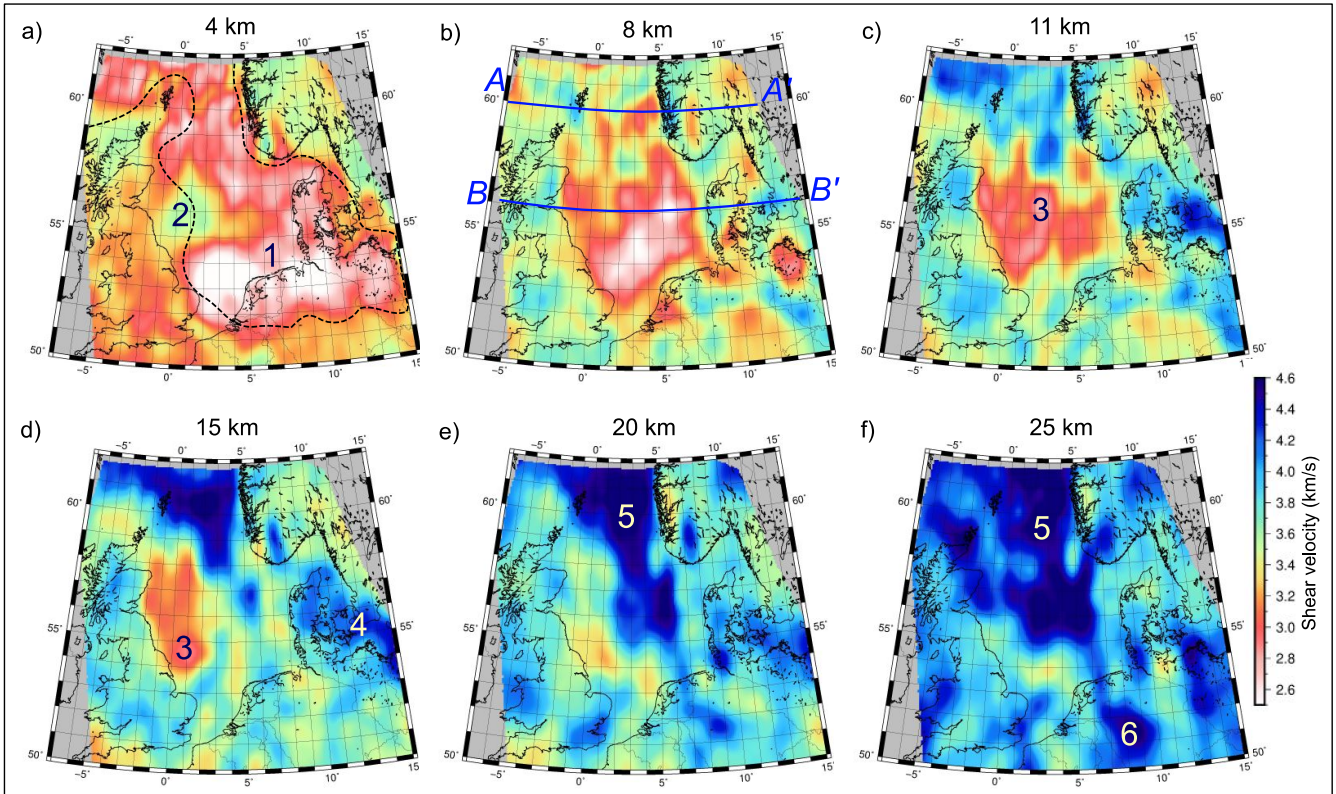


Fig. 7: Depth slices through the new 3D shear-wave velocity model of the North Sea and surrounding landmasses at depths of 4, 8, 11, 15, 20 and 25 km. Labeled velocity anomalies '1-6' are discussed in the text. Dashed black line on (a) marks 4 km sediment thickness contour from EuCRUST-07 (Tesauro et al., 2008). A-A' and B-B' are the location of cross-section slices shown in Figure 6. See Supplementary Fig. 7 for slices at 30, 35 and 40 km depth.

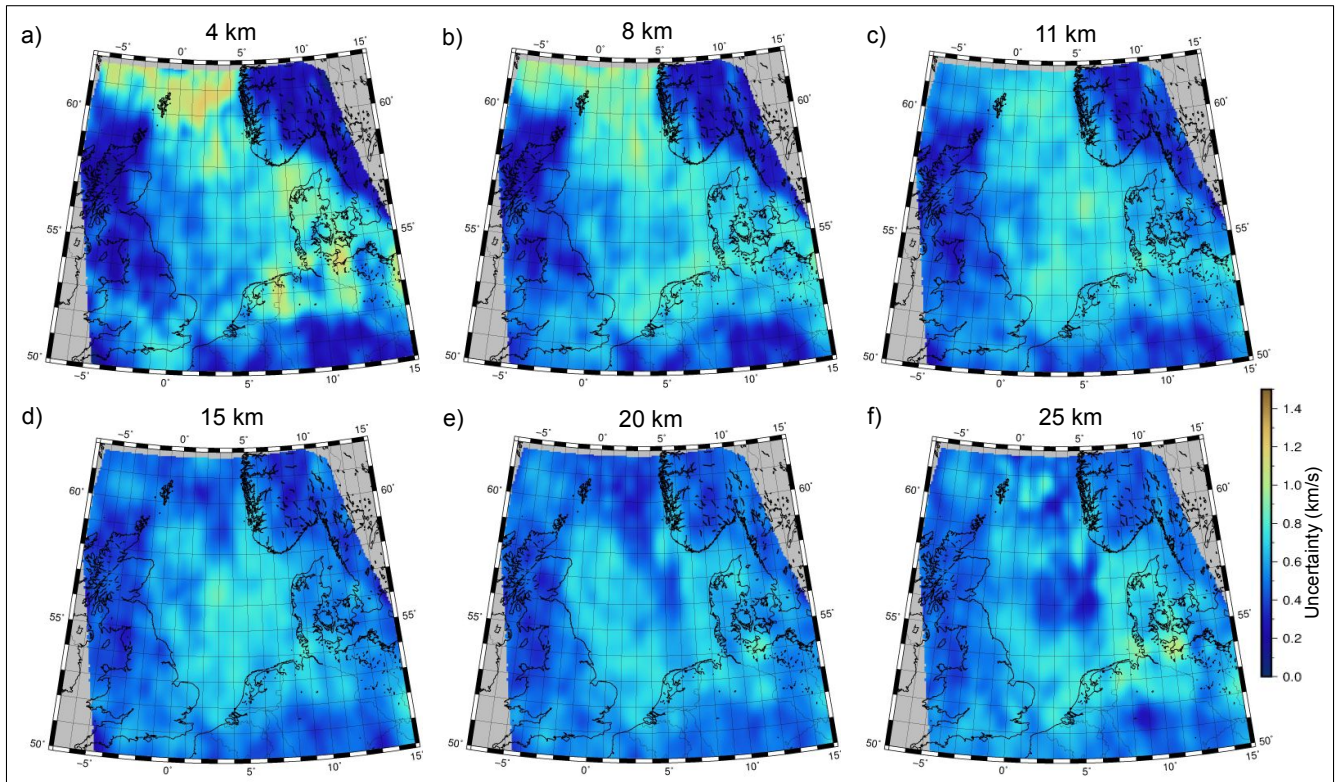


Fig. 8: Associated standard deviation values for the mean velocity model shown in Figure 4. Additional slices at 30, 35 and 40 km depth are shown in Supplementary Fig. 7.

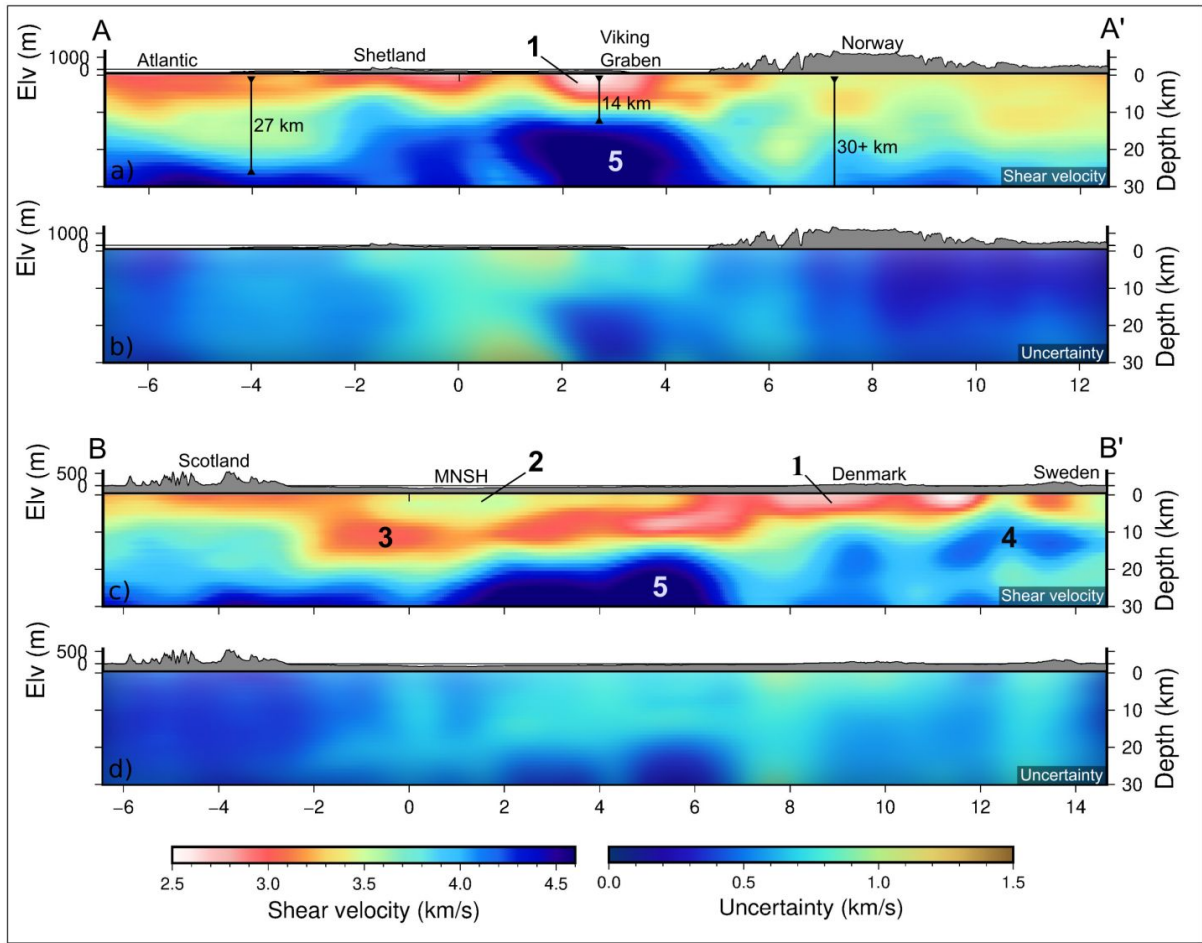


Fig. 9: Cross-section slices through the new 3D shear-wave velocity model of the North Sea and surrounding landmasses at latitudes of 56.0° and 60.0°. Labelled velocity anomalies '1-5' are discussed in the text. Associated standard deviation values for the velocity model are shown below each cross-section. MNSH: Mid North Sea High.

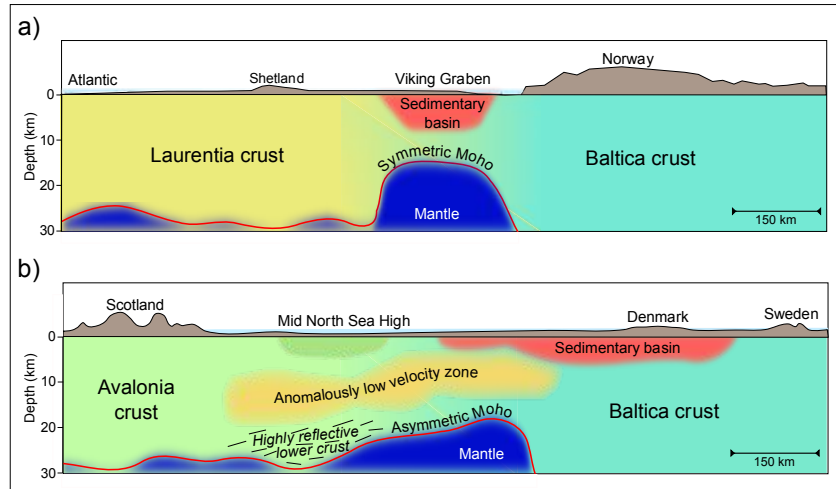


Fig. 10: Cartoon summarising the key interpretations of this study. (a) symmetric thinning of the crust in the northern North Sea between crust of Laurentia and Baltica origin; (b) asymmetric thinning of the crust of Avalonia and Baltica origin with an anomalously low velocity zone above highly seismically reflective lower crust around the Mid North Sea High region.

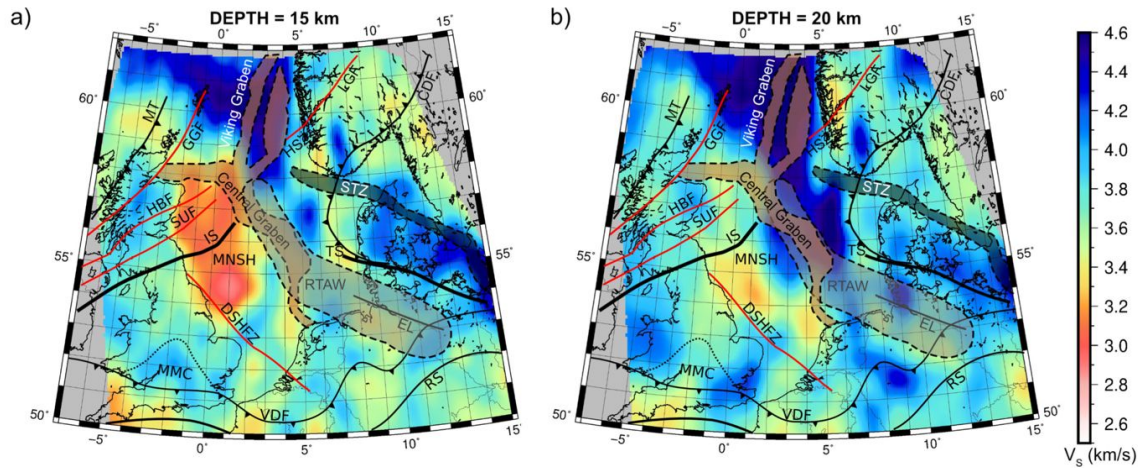


Fig. 11: Major crustal and tectonic features in the study area overlain onto depth slices through the final S-wave velocity model at: a) 15 km; and b) 20 km. MT: Moine Thrust; GGF: Great Glen Fault; HBF: Highland Boundary Fault; SUF: Southern Uplands Fault; IS: Iapetus Suture; MNSH: Mid-North Sea High; DSHFZ: Dowsing South Hewett Fault Zone; MMC: Midlands Micro-Craton; VDF: Variscan Deformation Front; RS: Rhenish Massif; EL: Elbe Lineament; TS: Thor Suture; STZ: Sorgenfrei-Tornquist Zone; HSZ: Hardangerfjord Shear Zone; LGF: Lærdal-Gjende Faults; CDF: Caledonian Deformation Front. The Remnant Thor Accretionary Wedge (RTAW) shaded grey is a low P-wave velocity region (after Smit et al., 2016) and brown shading denotes regions of major Late Palaeozoic-Mesozoic extension (after Fazlikhani et al., 2017).

Supplementary material for:

Controls on the development and termination of failed continental rifts: Insights from the crustal structure and rifting style of the North Sea via ambient noise tomography

E. Crowder^{1,*}, N. Rawlinson², D. G. Cornwell¹, C. Sammarco¹, E. Galetti⁴, A. Curtis^{3,4}

1. School of Geosciences, University of Aberdeen, Aberdeen AB24 3UE, Scotland, United Kingdom
2. Department of Earth Sciences, University of Cambridge, Cambridge, CB3 0EZ, United Kingdom
3. School of Geosciences, University of Edinburgh, Edinburgh, EH8 9XP, United Kingdom
4. Institute of Geophysics, ETH Zurich, Zurich, Switzerland

* Corresponding author. Email address: emily.crowder@abdn.ac.uk (E. Crowder)

Content of this file:

Supplementary figures

Figure S1

Figure S2

Figure S3

Figure S4

Figure S5

Tomographic inversion parameters

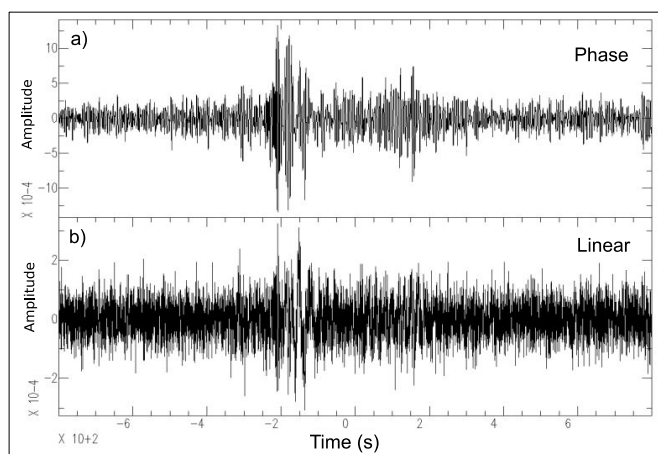


Figure S1: Linear stack of all daily cross-correlations between station pairs EDI and LWR using the phase cross-correlation method in (a) and a linear cross-correlation method with power value 1 in (b).

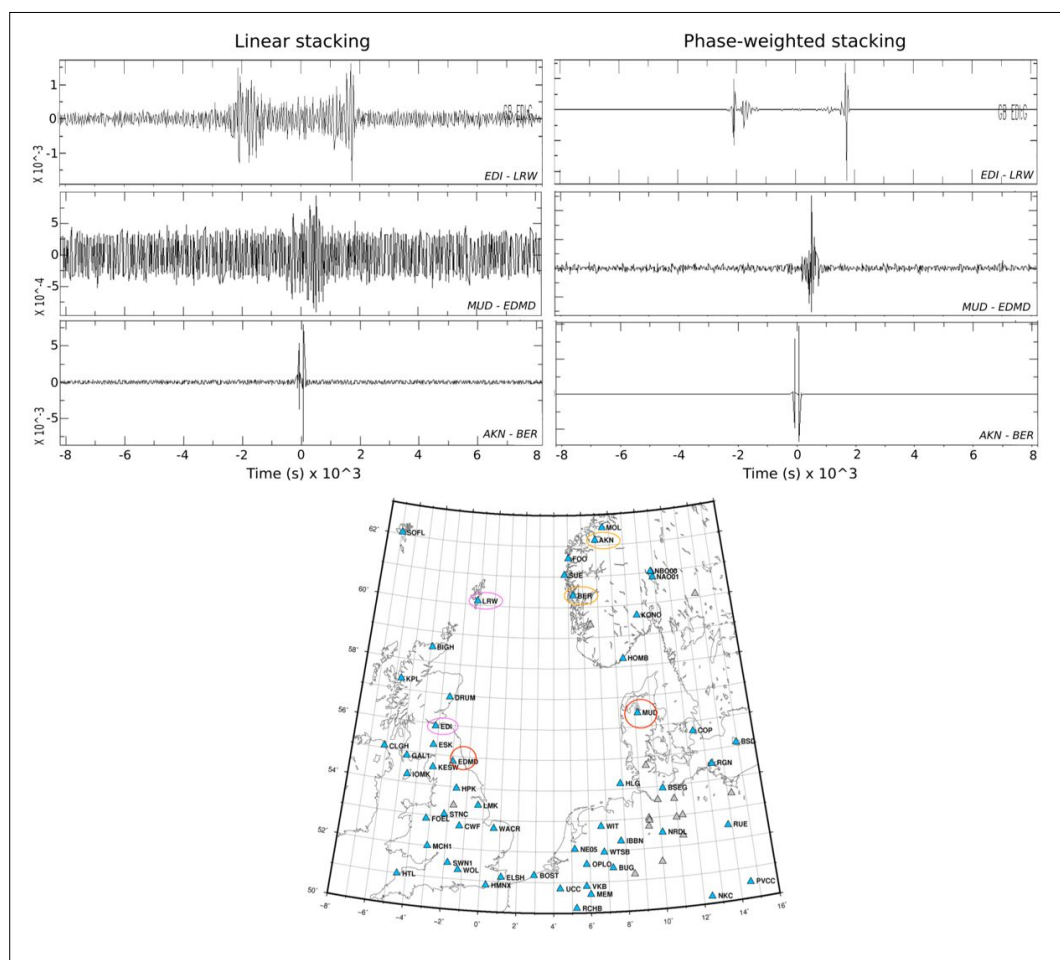


Figure S2: Comparison of linear and phase-weighted stacking methods for three example station pairs. The map below highlights the stations used in this example.

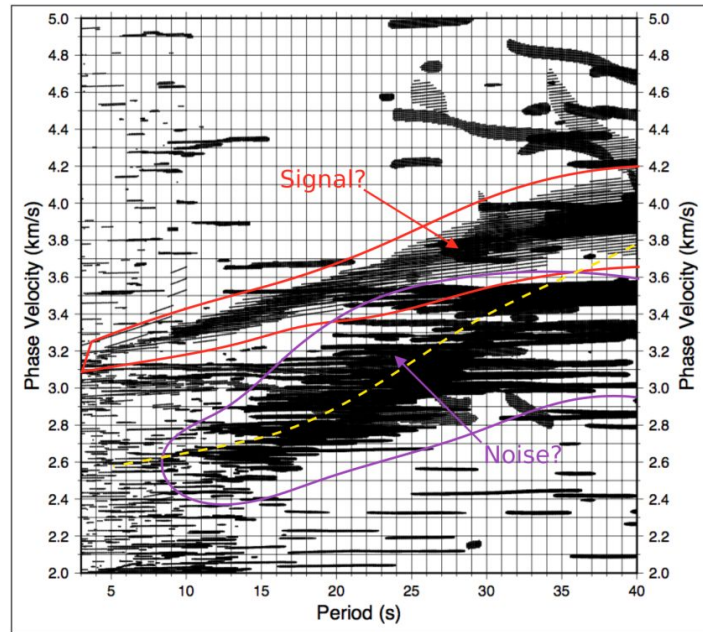


Figure S3: Phase dispersion plot created from automated frequency-time analysis using the image transformation technique. Average group velocity dispersion trend plotted as dashed yellow line for reference. Possible phase velocity signal shown outlined in red, with what may be noise highlighted in purple below.

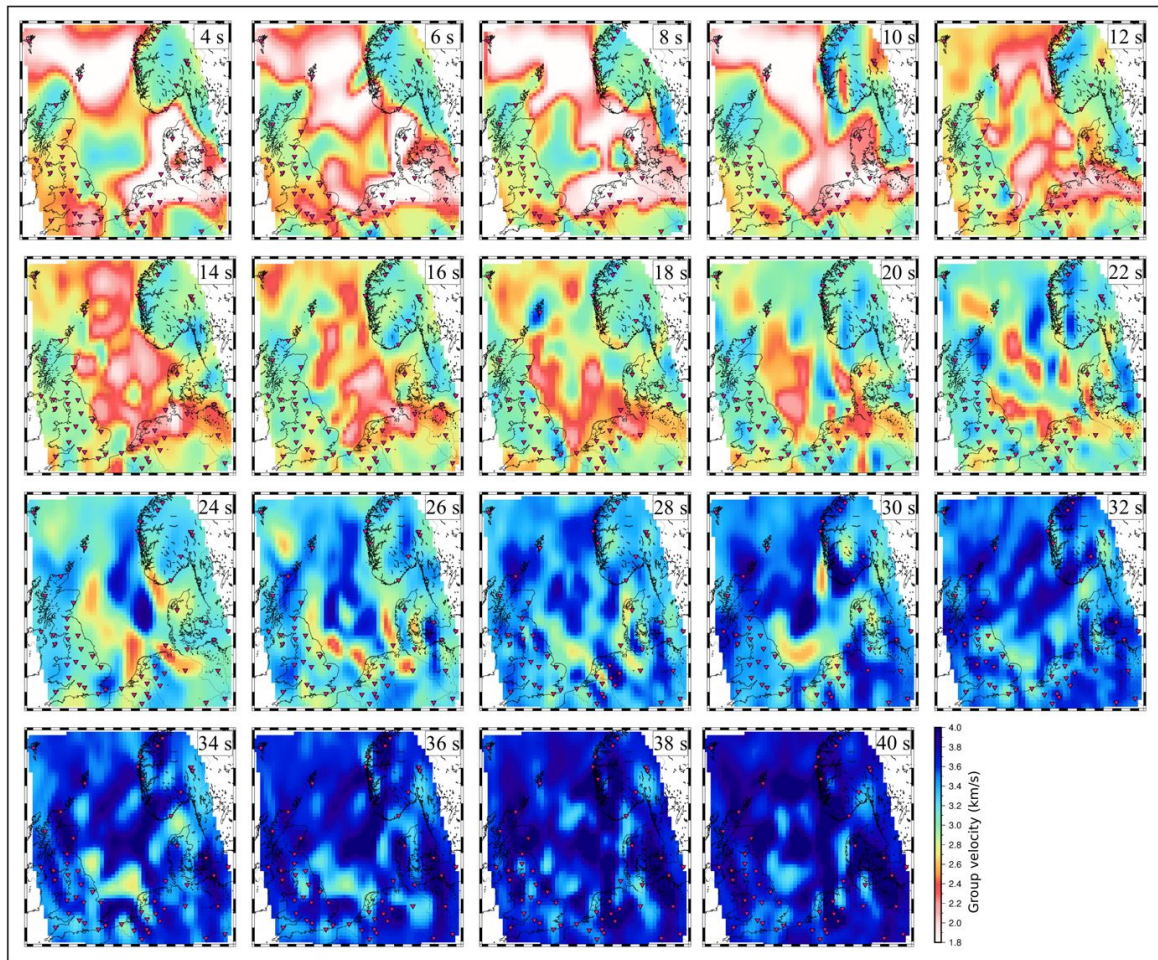


Figure S4: Group velocity maps of the North Sea and surrounding landmasses at even numbered periods from 4 to 40 s. Each pixel is associated with the regular grid of 2,903 points across the study area used to generate pseudo 1D group velocity dispersion curves.

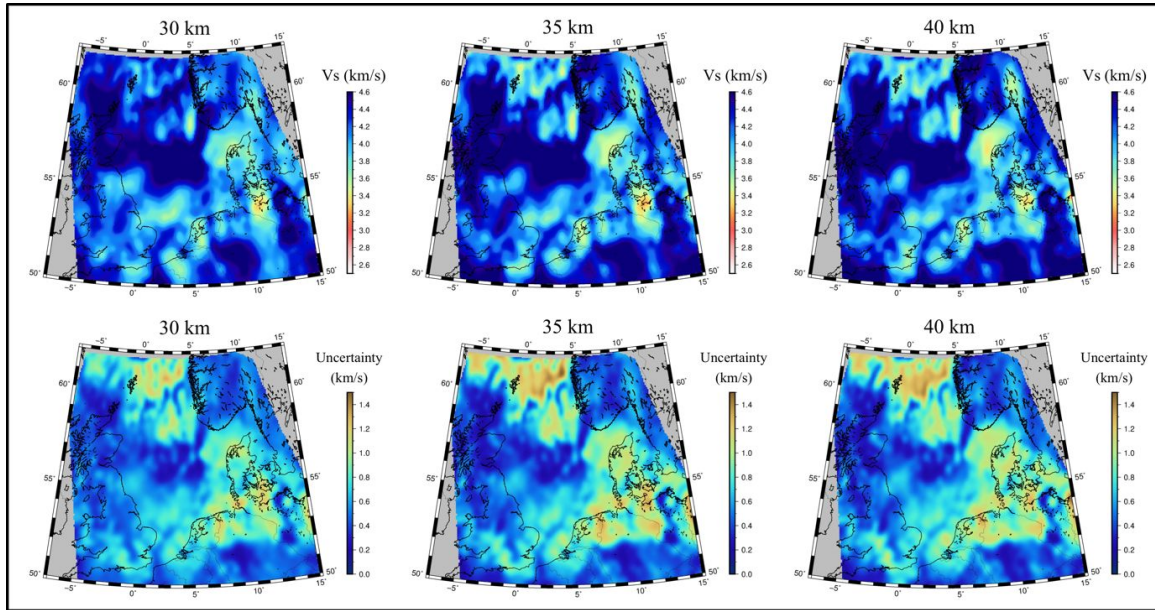


Figure S5: Depth slices taken through our new 3D shear-wave velocity model of the North Sea and surrounding landmasses at depths of 30, 35 and 40 km and their associated uncertainty estimates.

Inversion parameters for tomographic inversions

2D group velocity inversion priors

BURNIN= 100,000

The number of iterations to be discarded

TOTAL= 500,000 ,

The total number of iterations to run (per process in the MPI version)

THIN= 100 ,

Remaining models after burn-in sifted by taking every Nth model

MINPARTITIONS= 10 ,

The minimum number of partitions

MAXPARTITIONS= 400 ,

The maximum number of partitions

INITPARTITIONS= 200 ,

The initial number of partitions

JITTERPARTITIONS= 100 ,

For MPI only, jitter the number of initial partitions about *initpartitions*. in each process, the initial number of partitions will be uniformly distributed between *initpartitions - jitterpartitions* and *initpartitions + jitterpartitions*.

MINLON= -11.00 ,

Longitude bounds

MAXLON= 17.00 ,

Longitude bounds

MINLAT= 49.00 ,

Latitude bounds

MAXLAT= 63.00 ,

Latitude bounds

PD= 1.500 ,

The standard deviation for random partition moves

VS_MIN= Average velocity for given period + 0.75 km/s ,

Minimum velocity in each cell in km/s

VS_MAX= Average velocity for given period - 0.75 km/s ,

Maximum velocity in each cell in km/h

VS_STD_VALUE= 1.00,

1
2
3
4
5
6
7
8
9
10
11
12
13
14
15
16
17
18
19
20
21
22
23
24
25
26
27
28
29
30
31
32
33
34
35
36
37
38
39
40
41
42
43
44
45
46
47
48
49
50
51
52
53
54
55
56
57
58
59
60

The standard deviation for a change in velocity value

VS_STD_BD= 1.00 ,

For birth/death move, this is the standard deviation of the new cell's velocity value

SIGMA_MIN= 1.00 ,

Minimum value of noise parameter

SIGMA_MAX= 50.00 ,

Maximum value of noise parameter

SIGMA_STD= 1.00 ,

Standard deviation value of noise parameter

The code is open source and can be downloaded from here:

<http://www.earth.org.au/codes/rj-TOMO/>